Experimental Investigation of Wide Angle Bremsstrahlung in the H1 detector

von

Martin Hennecke

Diplomarbeit in Physik

vorgelegt der
Mathematisch-Naturwissenschaftlichen Fakultät
der

Rheinisch-Westfälischen Technischen Hochschule Aachen

im Dezember 1999

angefertigt im
I. Physikalischen Institut

Prof. Dr. Ch. Berger

Contents

Chapter 1

Introduction

Among all natural sciences physics is the royal one. It is the only discipline including excellent theories[1]. Its three frontiers are the physics of the "infinitely" big (cosmology), the "infinitely" complicated (chaotic systems) and the "infinitely" small (particle physics). The aim of the latter one is a theory of matter which unifies all known forces to just one interaction. Apart from being simple it should give a good quantitative description of all observable phenomena. The current theory of particle physics is the standard model. It assumes matter to consist of few elementary particles, an idea which was first introduced by Democritus[2].

1.1 The Standard Model

Today we believe matter to consists of fundamental fermions[3], i. e. quarks and leptons. Due to their properties both are classified in three families (See table 1.1). The standard model is based on gauge theories [2] which rely on certain symmetries and broken symmetries. Therefore left handed fermions are combined to isodubletts and the right handed ones to isosingletts according to the symmetry group $\mathrm{SU}(2)_T \times \mathrm{U}(1)_Y$, where T denotes the weak isospin and Y represents hypercharge. In addition to the electric charge quarks carry colour charge. This quantum number can either be red, green or blue because quarks are a colour triplet under $\mathrm{SU}(3)_C$ transformation where C indicates colour. Particles which consists of quarks are called hadrons.

The underlying symmetry of the standard model is the product of the three groups $\mathrm{SU}(3)_C \times \mathrm{SU}(2)_T \times \mathrm{U}(1)_Y$. The standard model also contains the antiparticles of quarks and leptons having the same multiplicative but opposite additive quantum numbers. The interactions described by the standard model are the strong, the electromagnetic and the weak interaction. All three are invariant under gauge transformations and described by quantum field theories [3, 4]. The latter two have been unified to the electroweak interaction, also called GSW model [5, 6, 7]. The exchange particle of the electromagnetic interaction described by QED[4] is the photon. It couples to electric charges. The field

[1] In [1] R. Penrose classifies all known theories as being excellent, useful or unproven.

[2] Greek philosopher, 460-370 BC.

[3] Fermions are particles with half integer spin. Particles with integer spin are called bosons.

[4] Quantum Electro Dynamics

Leptons (Spin 1/2)	$\begin{pmatrix}\nu_e\\ e^-\end{pmatrix}_L$ $\begin{pmatrix}\nu_\mu\\ \mu^-\end{pmatrix}_L$ $\begin{pmatrix}\nu_\tau\\ \tau^-\end{pmatrix}_L$ e^-_R, μ^-_R, τ^-_R
Quarks (Spin 1/2)	$\begin{pmatrix}u\\ d\end{pmatrix}_L$ $\begin{pmatrix}c\\ s\end{pmatrix}_L$ $\begin{pmatrix}t\\ b\end{pmatrix}_L$ u_R, d_R, c_R, s_R, t_R, b_R
Gauge Bosons (Spin 1)	γ, Z^0, $W^\pm$, 8 gluons g
Skalar (Spin 0)	*Higgs*

Table 1.1: The particles of the standard model.

quanta of the weak interaction are the $W^\pm$ and the Z^0 bosons. These couple to all leptons and quarks. The strong interaction whose underlying theory is QCD[5] is mediated by gluons which carry colour charge. These couple to quarks and, unlike photons, to each other.

The scalar Higgs particle [8, 9] is predicted by the standard model but all searches have been unsuccessful so far. It is introduced by the mechanism of spontaneous symmetry breaking and could explain the generation of particle masses. Its own mass is expected to be less than 1 TeV.

1.2 Beyond the Standard Model

Although the standard model has proven to be successful in describing experimental data there are still many open questions. One is the problem of gravity which up to now is not included in the standard model. Gravity is described by general relativity [10] which counts among the classical theories. Today it is not possible to quantise it with standard methods because of the necessity of Spin 2 gravitons[6]. They would lead to a theory which is not renormalizable and hence fails in describing nature.
Other open questions are:

- Why is the charge ratio of quarks and charged leptons exactly 1/3 and why is the number of both lepton and quark generations equal to three ?
- There is no explanation for the symmetry of quarks and leptons w. r. t. the electroweak interaction.
- The theory relies on 18 free parameters which have to be taken from measurements. They cannot be calculated from the standard model in the first place.
- The scalar Higgs particle gives rise to the so called hierarchy problem. This term refers to the instability of the Higgs mass against radiative corrections. A Higgs mass in the order of 1 TeV requires a fine tuning of two parameters over 24 significant digits. It is hard to believe that this fine tuning is realized in nature.

[5] Quantum Cromo Dynamics
[6] However this can be achieved by means of the string theory.

Various theories exist which try to solve the problems of the standard model. They all have in common the fact that they contain the standard model as a low energy approximation.

Grand Unification Theories (GUT)

Grand Unification Theories[11, 12] unify QCD and the electroweak interaction. This is achieved by introducing a new symmetry group. They have to cope with the hierarchy problem, i. e. the distance between the electroweak symmetry breaking ($\approx 10^2$ GeV) is far away from the scale of grand unification ($\approx 10^{19}$ GeV).

Compositeness models

Compositeness theories assume fermions to have substructure. Hence they reduce the number of elementary particles. These are called preons or rishons [13]. Compositeness models give a solution for the generation problem. Masses could arise from the dynamics of the new postulated particles. Unfortunately these models come into conflict with the Heisenberg uncertainty principle. Confining the constituents to a sphere of radius $R < 10^{-18}$ m leads to a momentum uncertainty of 200 MeV [14]. This exceeds the mass of many of the present fundamental particles.

Technicolour models

In technicolour models the Higgs boson consists of two new technifermions. This assumption can perhaps solve the hierarchy problem.

Supersymmtery (SUSY)

These theories assign a fermion to each boson, hence duplicating the number of fundamental particles [15]. Supersymmetric models maybe can solve the hierarchy problem and quantise gravitation. For instance, the supersymmetric partners of leptons and quarks are sleptons and squarks[7]. The masses of the new supersymmetric particles are expected to be less than 1 TeV.

Stringtheory

String theories [16, 17] abandon the idea of pointlike fundamental particles. Instead they change to extended one dimensional objects, the so called strings. These vibrate in a D dimensional space. Today the number D of dimensions is believed to be 10 or 11. The approach of extended objects has the advantage of removing divergencies out of the theory. String theory includes all known interactions and quantum gravity. It provides a finite number of massless states (S=0 $\rightarrow$ Higgs, ..., S=2 $\rightarrow$ graviton) and an infinite number of massive excitations. The 5 existing string theories maybe can be unified to the so called M theory.

[7] The prefix 's' stands for the term scalar, i.e. spin 0.

1.3 Motivation

The reaction investigated in this study is wide angle bremsstrahlung $ep \to ep\gamma$. It is one of the simplest reactions which can be studied at the HERA ep collider. It allows to test our understanding of QED with experimental data.
In addition one can extend previous searches for excited electrons e^* [18, 19] predicted by compositeness models. Their discovery would be a proof of electron substructure.
The analysis is based on data taken from 1995 to 1997 as well as 1999, corresponding to a total luminosity of $\mathcal{L} \approx 41.6\,\mathrm{pb}^{-1}$.

The thesis is organized as follows: Chapter 2 gives an overview over the ep collider HERA and the H1 detector. In chapter 3 the theory of wide angle bremsstrahlung is presented as well as the corresponding background processes. Special attention is given to the production of excited electrons. The fourth chapter describes the Monte Carlo generators which were used in this study. Chapter 5 explains the analysis. The results are compared with the expectation obtained from Monte Carlo studies. In chapter 6 exclusion limits for the production of excited electrons are calculated. The last chapter summarizes and gives an outlook on how to proceed in the future.

Chapter 2

HERA and the H1 Detector

2.1 The Storage Ring HERA

The storage ring HERA[1] is an unique device for the head-on collision of electrons [2] and protons at high energies. Being in operation since 1992 it consists of two independent accelerators situated in a 6.3 km circular tunnel below Hamburg. Protons are injected at 40 GeV and subsequently accelerated to 920 GeV [3] whereas electrons are injected at 12 GeV and acccelerated to 27.5 GeV. Electrons and protons have their own system of pre-accelerators, respectively. The beams collide in two interaction points situated in the north and south hall of HERA, each of which is surrounded by a multi-purpose particle detector (See Fig.2.1). Each beam consists of ≈ 210 particle bunches of which ≈ 32 are so called pilot bunches. These pilot bunches have no partner bunch for collision in order to determine the backround rate of residual gas atoms interacting with the beams. The time separation between two bunches is 96 ns leading to an interaction frequency of $\approx 10.4\,\mathrm{MHz}$. After the injection the beam currents are $\sim$76 mA for the protons and $\sim 30\,\mathrm{mA}$ for the electrons.(See Table.2.1). Proton fill lifetimes are of the order of 24 h, while the duration of an electron fill is about 12 h.

2.2 The H1 Detector

A short overview of the main detector components used in this analysis will be given here. Further parts are described briefly in section 2.2.5. A complete description of the H1 detector can be found in [20].

2.2.1 Overview

The H1 detector is a multi-purpose particle experiment situated in the north hall of the HERA collider (See Fig.2.2). It was designed to identify leptons and hadron jets

[1] Hadron Elektron Ring Anlage

[2] To be succinct, the distinction between electrons and positrons will be dropped in this thesis since the investigated processes are independent of the lepton type. The word "electron" will be used generically to refer to both e^- and e^+, unless explicitly stated.

[3] After the shutdown period '97/'98 the proton energy was increased from 820 GeV to 920 GeV.

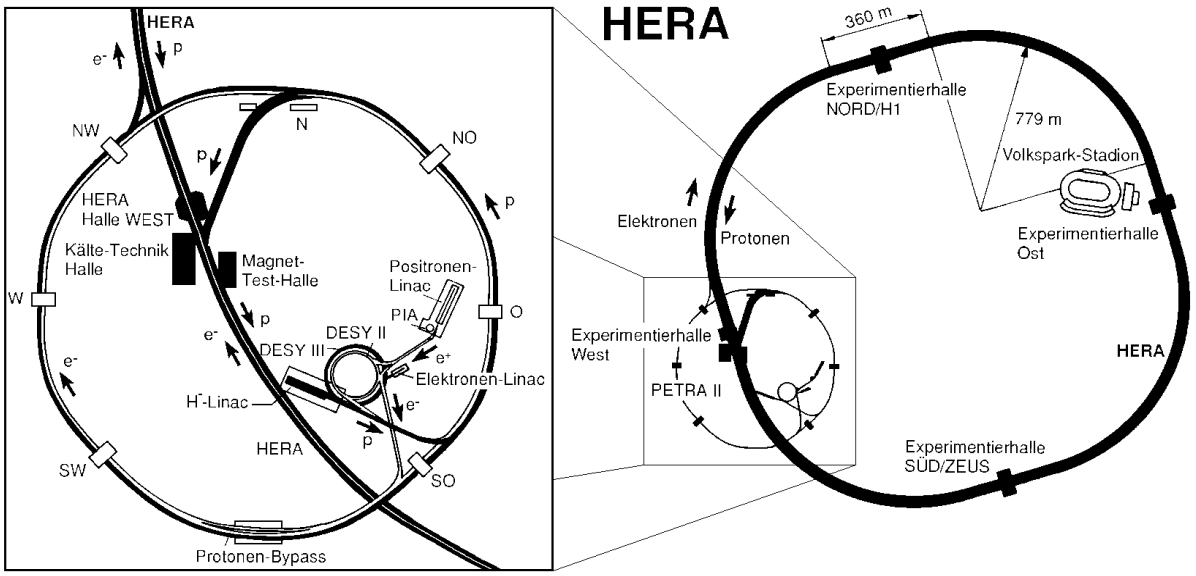

Figure 2.1: HERA and its pre-accelerators. The West Hall is occupied by the HERA-B experiment where the proton beam interacts with thin tungsten wires. Its aim is the investigation of b-Physics. The HERMES detector is based in the East Hall. Here the electron beam collides with a polarized gas target in order to probe the spin distribution inside the proton.

	Designparameter		Autumn 1992		
	p-Ring	$e^{\pm}$-Ring	p-Ring	$e^{\pm}$-Ring	Unit
Energy	820	30	820	26.7	GeV
Luminosity	1.5×10^{31}		3.0×10^{29}		$cm^{-2}s^{-1}$
Magnetic field	4.68	0.165	4.68	0.149	T
Number of particles	210	80	2.6	3.7	10^{11}
Current per bunch	760	290	241	101	μA
Number of bunches	210	210	10	10	
Bunch separation	96	96	96	96	ns
Injection energy	40	14	40	12	Gev
Filling time	20	15	120	30	min
σ_x/σ_y at interaction point	0.29/0.07	0.26/0.02	0.36/0.10	0.30/0.07	mm
σ_z at interaction point	110	8	≈ 200	≈ 10	mm
Energy loss per turn	6.2×10^{-6}	127			MeV
RF-Frequency	52.03/208.1	499.8	52.03	499.8	MHz

Table 2.1: Summary of HERA parameters (taken from [20]).

originating from ep collisions. At a center of mass energy of $\sqrt{s} \approx 300$ GeV the physics program accesible with HERA and H1 covers a wide range. The most prominent subjects are the determination of the proton structure function $F_2(x, Q^2)$ and tests of the standard model. H1 was planned as a so called 4π detector, i. e. it nearly covers the whole solid angle around the interaction point. In addition it has an onion like circular structure around the beam pipe [1]. In this way the majority of the produced particles can be detected within H1. The H1 detector has a coordinate system adjusted to the HERA collider. The directions of all particles are expressed by the azimuth angle θ and the polar angle ϕ. Its origin is the nominal interaction point, denoted WWP in Fig.2.4. The z axis or forward direction ($\theta = 0°$) is defined by the direction of the incoming protons. Hence the electrons fly into the backward direction ($\theta = 180°$). The x axis ($\theta = 90°, \phi = 0°$) is pointing into the center of the HERA collider and the y axis ($\theta = 90°, \phi = 90°$) points upwards. Due to the strongly imbalanced momenta of the incoming electrons and protons, most of the particles produced inside H1 are boosted into the forward direction. On average about 50% of them can be found in a cone where $\theta < 25°$. Therefore the H1 detector shows a clear asymmetry w. r. t. the z axis. More active material is placed in the proton direction then in the electron direction.

2.2.2 The Central Tracking System

The central tracking system of the H1 detector can be seen in fig. 2.3. Its purpose is the determination of tracks of charged particles. It is located around the beampipe and covers the polar angle range of $7° < \theta < 175°$. In order to achieve a high efficiency over the whole solid angle, the central tracking system has been divided into the forward (FTD) and central track detector (CTD). Both systems are optimized for their angular region. The momenta and angles of charged particles are measured to a precision of $\sigma_p/p^2 \approx 3 \times 10^{-3}\,\mathrm{GeV}^{-1}$ and $\sigma_\theta \approx 1\,\mathrm{mrad}$.

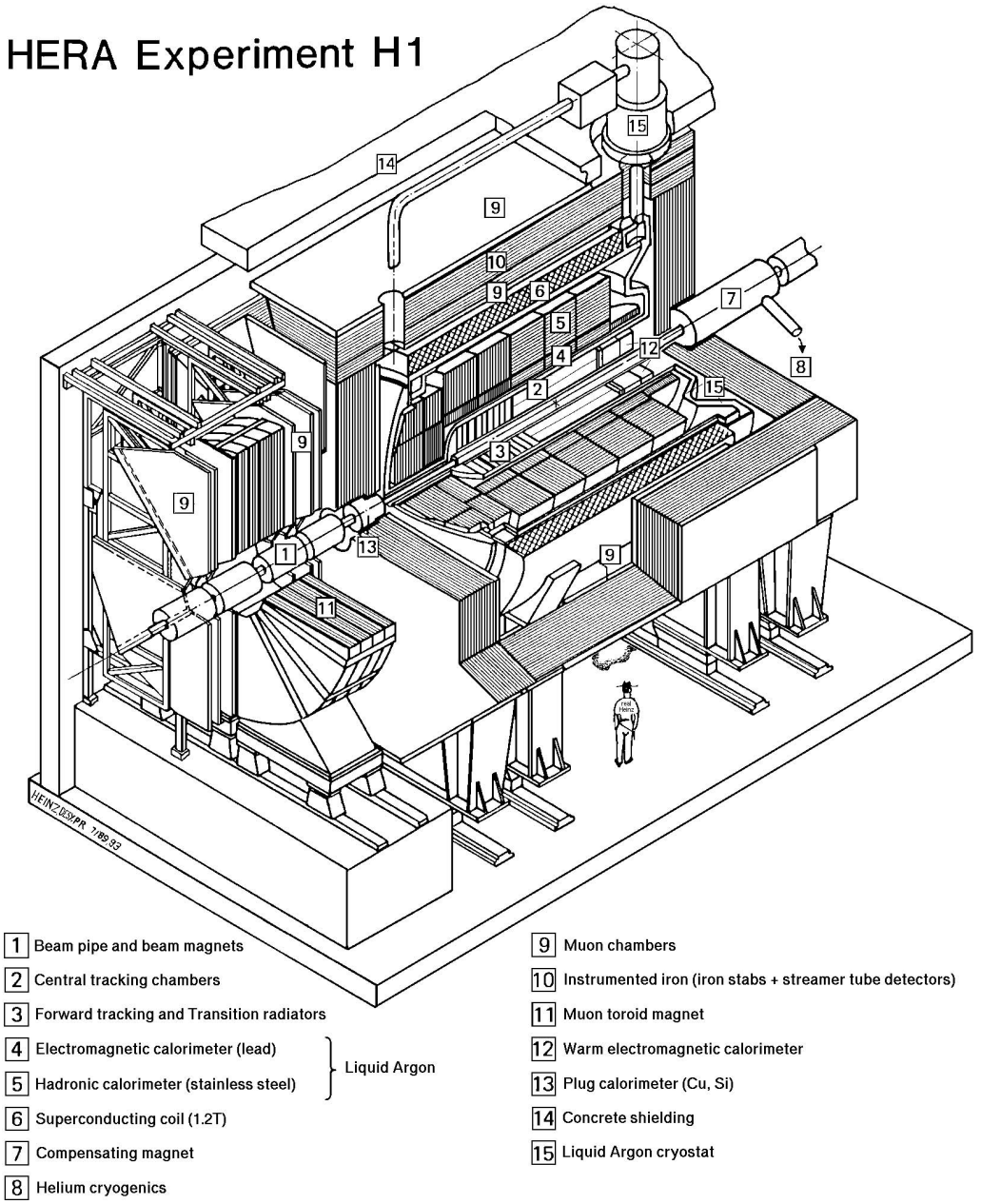

Figure 2.2: The H1 detector at HERA. Protons enter the detector from the top right corner whereas electrons come from the bottom left.

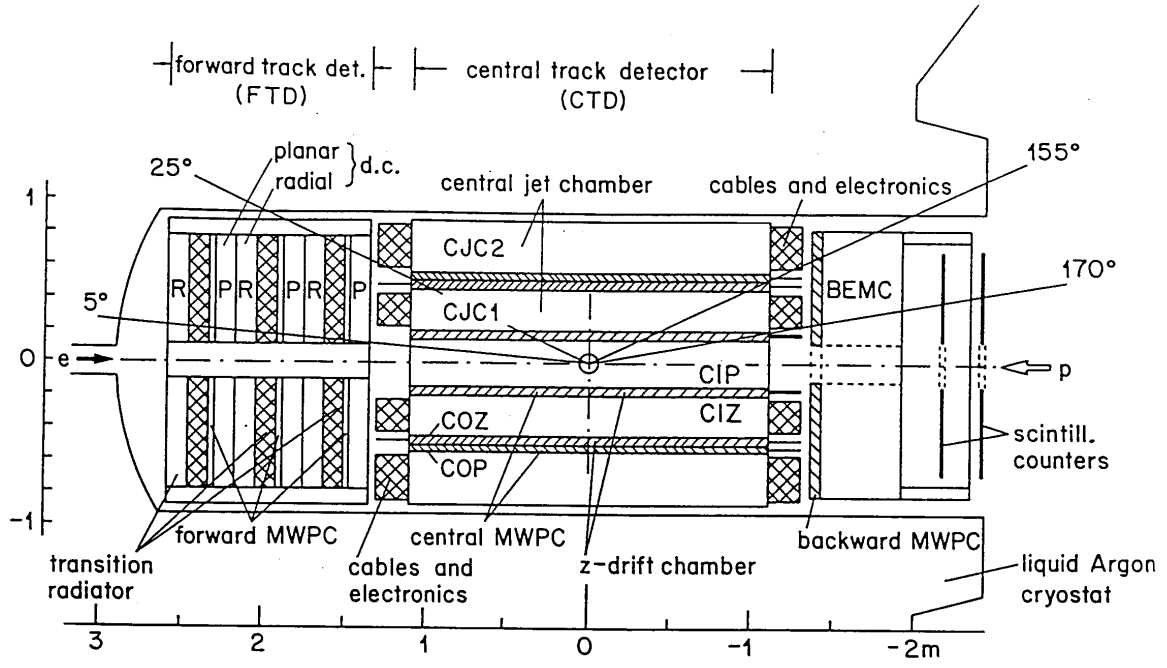

Figure 2.3: The H1 central tracking system. During the shutdown period '94/'95 the BEMC was replaced by a more sophisticated detector, the SpaCal.

Central track detector

The major components of the central track detector [2] are the central jet chambers, CJC1 and CJC2. These are two large concentric drift chambers consisting of 30 and 60 cells, respectively. Each drift cell is equipped with several (CJC1 24;CJC2 32) sense wires passing through parallel to the z-axis. The cells are inclined by about 30° w.r.t. the radial direction. The achieved space point resolution (r-ϕ-plane) is $\sigma_{r\phi} = 170\,\mu$m. By comparing the accumulated charges at both ends of the sense wires the precision of the z-measurement is $\sigma_z = 22\,$mm corresponding to 1% of the wire length.

The central inner (CIZ) and central outer (COZ) z-chambers have sense wires perpendicular to the z-direction. Their accuracy in measuring the z coordinate of a track is $\sigma_z = 300\mu m$. The central inner (CIP) and central outer (COP) proportional chambers are so called multi wire proportional chambers (MWPC). They provide space points for the vertex determination of the first level trigger.

Forward track detector

The forward track detector [3] consists of three identical parts. Each part comprises a planar drift chamber, a transition radiator and a radial drift chamber. In all drift chambers the sense wires run perpendicular to the beam axis, the planar ones having parallel wires whereas the radial drift chamber wires are radiating outwards from the beam pipe. The planar modules consist of three drift chambers rotated at 60° to each other in ϕ. In the transition radiators particles pass through 400 polypropylene foils producing transition

radiation photons. These soft x-rays are then detected in the radial modules.

2.2.3 The Liquid Argon Calorimeter

The liquid argon(LAr) calorimeter [4] [5] is the major detector component for the analysis described here. It is situated inside the main coil[4], between the central tracking system and the instrumented iron, and covers the angular range between $4° < \theta < 153°$. The whole calorimeter is embedded in a cryostat [15] filled with liquid argon and cooled down to a temperature of T = 90 K. It is made up of 8 detector wheels of which 7 are divided into an electromagnetic and a hadronic part (See Fig.2.4). The nomenclature of the wheels is given in Table 2.2.3. Each wheel consists of 8 identical stacks (See Fig.2.5).

Each cell of the e.m. stacks consists of 2.4 mm Pb absorber plates and 2.35 mm liquid argon gaps, the latter serving as active material. Each gap is equipped with a readout and a high voltage plane. The readout plane is divided into small pads collecting the produced charges in the liquid argon. The pads are merged to so called cells of which the LAr has 45.000 in total.

The cells of the hadronic stacks consist of 19 mm stainless steel and a double gap of liquid argon. In the middle they have a board with pads on both sides to collect the deposited charges. The e.m. part of the LAr extends over 20 to 30 radiation lenghts X_0 and the hadronic part over 5 to 8 interaction lengths λ, depending on the polar angle θ. This guarantees the complete absorbtion of the energy of incident electrons and photons.

The LAr is a non-compensating calorimeter, i. e. hadrons and electrons having the same energy produce a different signal amplitude[5]. Therefore electromagnetic and hadronic showers have to be identified as such and the corresponding scale factors must be applied. The energy resolution of the electromagnetic part of the calorimeter has been measured in test beams at CERN and found to be

$$\frac{\sigma_E}{E} = \sqrt{\frac{A^2}{E} + \frac{B^2}{E^2} + C^2} \tag{2.1}$$

where $A = 11\%\sqrt{E}$, $B = 154MeV$ and $C = 0.6\%$. The resolution of the hadronic part is also parametrized according to equation 2.1, with A = $(50.7\pm\ 0.1)\%\sqrt{E}$, B=0.9 GeV and C=$(1.6\pm0.1)\%$.

2.2.4 The Luminosity System

The H1 luminosity system enables the measurement of the absolute luminosity with an accuracy of $< 3\%$ as well as tagging of photoproduction events and energy measurement of photons from initial state radiation (ISR). It detects electrons and photons leaving H1 under small polar angles. The underlying physical reaction is the so called Bethe-Heitler process $ep \to ep\gamma$ [21]. It has the advantage of exact calculability, a high interaction and a low background rate. The main source of background is bremsstrahlung from the reaction $eA \to eA\gamma$, i. e. the electron emits a photon in the field of a residual gas atom. The rate

[4]The aim of this design was to reduce both the amount of dead material in front of the calorimeter and its overall size and weight.

[5]The charge output is $\sim 30\%$ less for hadrons than for electrons.

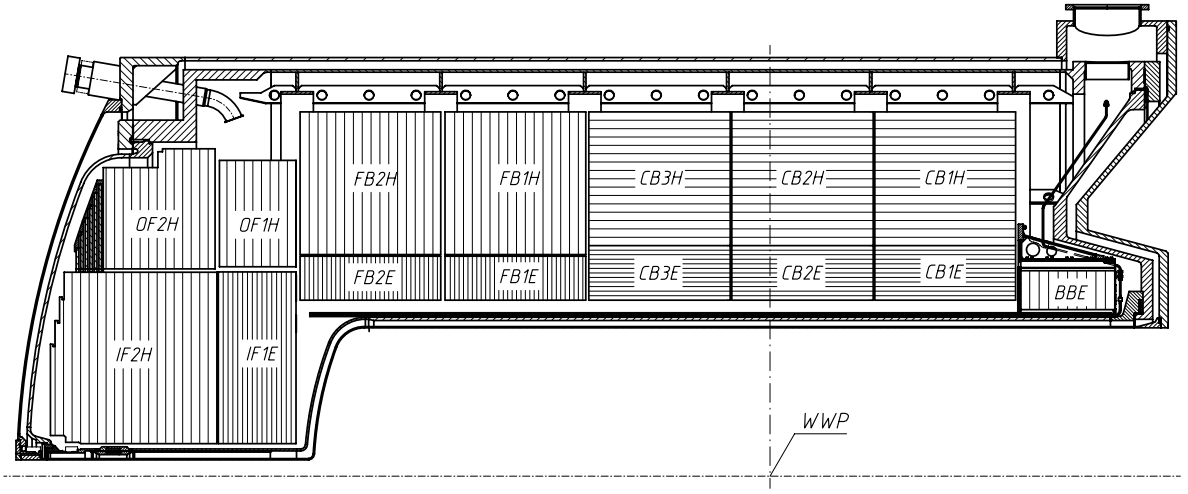

Figure 2.4: Longitudinal view of the liquid argon calorimeter. WWP denotes the nominal interaction point.

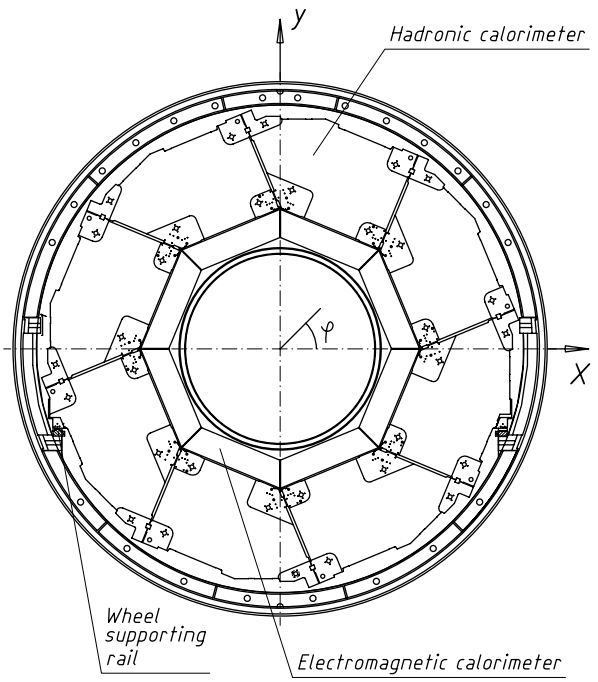

Figure 2.5: Radial view of a liquid argon calorimeter wheel in the r-ϕ plane.

BBE	Backward Barrel Electromagnetic
CBiE/H	Central Barrel Electromagnetic/Hadronic i=1,2,3
FBiE/H	Forward Barrel Electromagnetic/Hadronic i=1,2
IF1E	Inner Forward Electromagnetic
IF2H	Inner Forward Hadronic
OFiH	Outer Forward Hadronic i=1,2

Table 2.2: Nomenclature of the LAr calorimeter wheels

of these bremsstrahlung events comprises 10% of the $ep \to ep\gamma$ rate but can be subtracted by means of the pilot bunches (See Chapter 2.1). The luminosity system consists of two arms in which scattered electrons and photons are detected in coincidence.

The electron tagger (ET) and photon detector (PD) are situated close to the beamline at $z = -33.4\,\mathrm{m}$ and $z = -92.3\,\mathrm{m}$, respectively. The angular acceptance is $0 - 5\,\mathrm{mrad}$ for the electron tagger and $0 - 0.45\,\mathrm{mrad}$ for the photon detector. Both devices are crystal Čerenkov counters combined with photomultipliers for the readout. The basic layout of the luminosity system is shown in Fig.2.6. The absolute energy calibration can be performed with a precision of better than 1%. This is due to the fact that the electron and photon energies are correlated, namely

$$E_{ET} + E_{PD} = E_{e-beam}.$$

2.2.5 Further Detector Components

The Superconducting Coil

The main solenoid [6] produces an almost homogeneous magnetic field inside the central tracking system. The average value of the z-component B_z over the tracker volume is 1.15 T. The nominal magnet current is 5514 A at a voltage of 12 V. Liquid helium is used as coolant.

The SpaCal

The SpaCal[6] [12] has replaced the former BEMC[7] during the detector upgrade in the shutdown period 94/95. The reason was the wish for an increased efficiency and energy resolution as well as the identification of hadrons and electrons. Therefore the SpaCal is divided into a hadronic and an electromagnetic section, the latter being closer to the interaction point. It consists of alternating layers of scintillating fibres and lead absorber plates. The angluar range covered is $151° < \theta < 177°$.

[6] Spaghetti Calorimeter
[7] Backward Electromagnetic Calorimeter

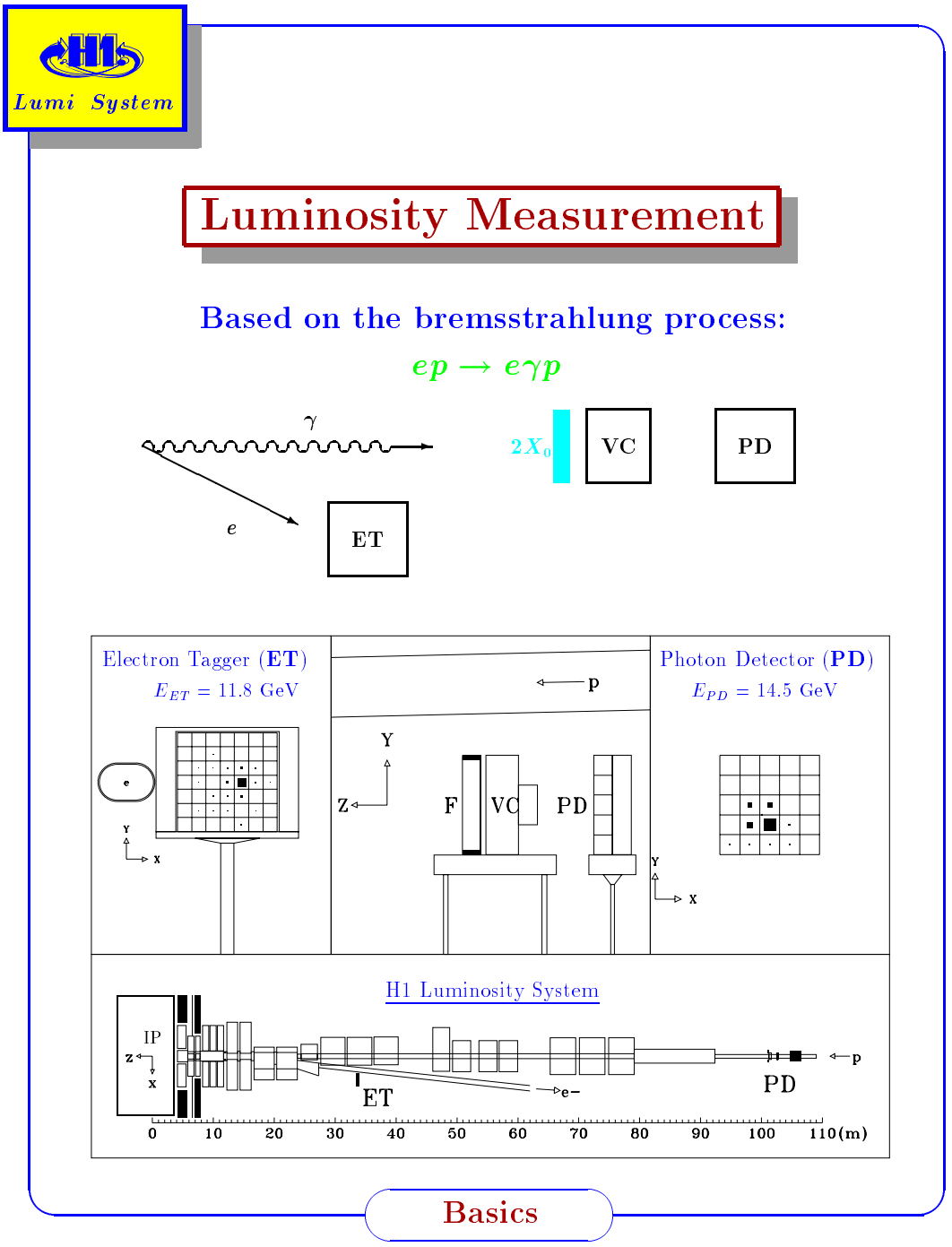

Figure 2.6: Basic layout of the H1 luminosity system as described in chapter 2.2.4.

The Plug Calorimeter

The plug calorimeter [13] closes the gap between the beam pipe ($\theta \approx 0.6°$) and the LAr calorimeter ($\theta \approx 3.5°$). Its purpose is the detection of hadrons leaving H1 close to the beam pipe.

Central Muon Detector

Since muons are penetrating particles, i. e. they easily cross the inner parts of H1 without being absorbed, the central and forward muon system are the outermost detector components. The central muon detector [9] [10] is embedded in the iron yoke which is used for guiding the B field flux of the main solenoid. It consists of limited streamer tubes inserted in the gaps of the instrumented iron and serves for the detection of penetrating particles.

Forward Muon System

The forward muon system [9] [11] was designed for the determination of high momentum muons between 5 GeV/c and 200 GeV/c. Therefore is covers the angluar range between $3° < \theta < 17°$.

Time-of-flight

The time-of-flight counters (TOF) are used for the reduction of background events, taking advantage of the fact that particles from proton induced background and from ep collisions have a time separation of ~ 13 ns.

Chapter 3

Theoretical Foundations

3.1 Wide Angle Bremsstrahlung

The theory describing the investigated process of wide angle bremsstrahlung is presented in the following chapter. Section 3.1.1 gives an overview of the underlying physics. Section 3.1.2 describes the kinematics of the process. The cross sections are presented in section 3.1.3. The last section deals with the standard model background processes as well as the non standard model background of e^* production.

3.1.1 Introduction

Considering the reactions

$$ep \to e\gamma p \quad \text{and} \quad ep \to e\gamma X$$

depicted in fig. 3.1 one gets for the scattering amplitude, a priori

$$T \sim \frac{dq}{q^2 - m_e^2} \cdot \frac{dk}{k^2}$$

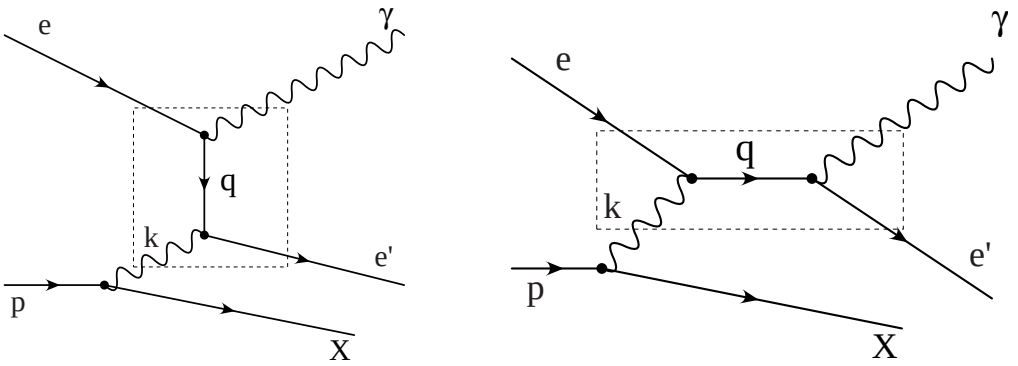

Figure 3.1: Feynman-diagrams for bremsstrahlung off the electron lines.

Obviously this amplitude is largely dominated by small values of both q^2 and k^2. According to the values of q^2 and k^2 one can distinguish three cases, where 0 stands for values of $\mathcal{O}(m_e^2)$.

$\mathbf{k^2 \to 0}$, $\mathbf{q^2 \to 0}$

The outgoing electron and photon as well as the hadronic system leave the detector along the beam pipe under small scattering angles, i. e. smaller than 1°. This configuration is called bremsstrahlung or Bethe-Heitler process. At low angles it leads to a large counting rate and is used for the luminosity measurement within H1. In principle it is the same reaction as the scattering of fast electrons in the coulomb potential of a nucleus.

$\mathbf{k^2}$ finite, $\mathbf{q^2 \to 0}$

This configuration corresponds to the so called radiative corrections in elastic ep scattering. Either the angle $\theta_{e\gamma}$ between the outgoing photon and the incoming electron or $\theta_{e'\gamma}$, the angle between the outgoing photon and electron is small. In both cases the photon energy E_γ is small as well.

$\mathbf{k^2 \to 0}$, $\mathbf{q^2}$ finite

The hadronic system leaves the detector along the beam pipe. The scattered electron and photon are detected at large ("wide") polar angles which leads to the term wide angle bremsstrahlung. Because k^2 is small, one can decompose the cross section into two factors: a flux factor which replaces the incoming proton by a photon beam and the known cross section of the Compton effect which takes place inside the hashed boxes of fig. 3.1. Therefore this reaction is also known as QED Compton or quasi-real QED Compton process because of the quasi-real photon with $k^2 \approx 0$ exchanged by the electron and the proton. The method of factorization can also be applied to the most general case where both q^2 and k^2 are finite[1], i. e. greater than m_e^2.

In addition it is conventional to classify the process $ep \to e\gamma X$ according to the value of $W = m_X$, the invariant mass of the outgoing hadronic system.

Elastic contribution: $\mathbf{W = m_p}$

In the elastic case $ep \to e\gamma p$ where $k^2 \approx 0\,\mathrm{GeV}^2$, the incoming proton does not become excited and stays intact. Hence W is equivalent to the proton mass m_p.

Resonant contribution: $\mathbf{m_p < W < 1.8\,GeV}$

The reaction $ep \to e\gamma R$, where R represents a resonance state, is also called quasi-elastic. Here the value of k^2 is less than $5\,\mathrm{GeV}^2$. It is dominated by the three resonances $\Delta(1236)$, N*(1520) and N*(1688). Their parameters can be found in table 3.1.

[1] This approach is used by the new QED Compton generator WABGEN described in chapter 4.1.

	Δ	N*	N*
m_R (GeV)	1236	1520	1688
Γ_R (MeV)	120	120	120

Table 3.1: Characteristics of the three most important resonances.

Inelastic contribution: W > 1.8 GeV

In the process $ep \to e\gamma X$ one can assume the quark model to be valid for $k^2 > 5\,\mathrm{GeV}^2$ and $\xi < 0.99$. ξ is the momentum fraction of the incoming proton carried by the struck quark and defined by

$$\xi = \frac{k^2}{k^2 + W^2}.$$

3.1.2 Kinematics

For $k^2 \approx 0\,\mathrm{GeV}^2$ the kinematics of the WAB process is over constrained. Making few assumptions and taking advantage of energy and momentum conservation the energy of the detected electron and photon as well as their invariant mass $m_{e\gamma}$ can be calculated simply by the polar angles θ_e and θ_γ. These assumptions are:

- the virtual photon emitted by the proton and the proton itself are collinear, i. e. $k^2 \approx 0\,\mathrm{GeV}^2$
- in the plane perpendicular to the beams the electron and the photon are separated by $\Delta\phi \approx 180°$
- electron and proton mass as well as initial state radiation are neglected.

The 4-momenta are given by

$$e = E_e \begin{pmatrix} 1 \\ 0 \\ 0 \\ -1 \end{pmatrix}, p = E_p \begin{pmatrix} 1 \\ 0 \\ 0 \\ 1 \end{pmatrix}$$

for the initial particles and

$$e' = E'_e \begin{pmatrix} 1 \\ \sin\theta_e \\ 0 \\ \cos\theta_e \end{pmatrix}, \gamma' = E'_\gamma \begin{pmatrix} 1 \\ -\sin\theta_\gamma \\ 0 \\ \cos\theta_\gamma \end{pmatrix}$$

for the outgoing ones [2]. The 4-momentum of the virtual photon collinear to the proton is

$$\gamma = z E_p \begin{pmatrix} 1 \\ 0 \\ 0 \\ 1 \end{pmatrix}.$$

[2]For this calculation the angles ϕ_e and ϕ_γ are neglected. The result is independent of a rotation of the x-y plane.

Four-momentum conservation leads to

$$e + \gamma = e' + \gamma'.$$

Inserting the corresponding vectors gives a set of three equations:

$$\begin{aligned} E_e + zE_p &= E'_e + E'_\gamma && (3.1)\\ 0 &= E'_e \sin\theta_e - E'_\gamma \sin\theta_\gamma && (3.2)\\ -E_e + zE_p &= E'_e \cos\theta_e - E'_\gamma \cos\theta_\gamma. && (3.3) \end{aligned}$$

Subtracting eqn. 3.1 from eqn. 3.3 eliminates the unknown fraction of the proton momentum carried by the photon:

$$2E_e = E'_e(1 - \cos\theta_e) + E'_\gamma(1 - \cos\theta_\gamma). \quad (3.4)$$

Combining eqn. 3.2 and eqn. 3.4 and solving for E_e and E_γ gives

$$\begin{aligned} E'_e &= \frac{2E_e \sin\theta_\gamma}{(1-\cos\theta_\gamma)\sin\theta_e + (1 - \cos\theta_e \sin\theta_\gamma)}\\ E'_\gamma &= \frac{2E_e \sin\theta_e}{(1-\cos\theta_\gamma)\sin\theta_e + (1 - \cos\theta_e \sin\theta_\gamma)}. \end{aligned}$$

As one can see E_e and E_γ only depend on θ_e and θ_γ. Making the assumptions mentioned earlier it is hence possible to determine the energy of the outgoing particles by measuring their polar angle in the lab frame. The invariant mass is given by

$$\begin{aligned} m^2_{e\gamma} &= (e' + \gamma')^2 && (3.5)\\ &= 2e'\gamma' && (3.6)\\ &= 2E'_e E'_\gamma(1 + \sin\theta_e \sin\theta_\gamma - \cos\theta_e \cos\theta_\gamma). && (3.7) \end{aligned}$$

Taking the previous equations into account, eqn. 3.7 can be transformed to

$$m^2_{e\gamma} = 4E_e^2 \frac{1+\beta}{1-\beta}.$$

Beta is the boost of the $e\gamma$-CMS into the z direction measured in the lab frame and defined by

$$\beta = \frac{\sin(\theta_e + \theta_\gamma)}{\sin\theta_e + \sin\theta_\gamma}.$$

For $m_{e\gamma} > 2E_e$ β is positive and for $m_{e\gamma} < 2E_e$ the Lorentz boost is negative. Hence, electron and photon are boosted into the forward direction predominantly if $m_{e\gamma}$ is large. Since the type of the coupling did not enter the calculation it is also valid for the $e^* \to e\gamma$ decay which will be explained in section 3.2.5. For large e^* mass electron and photon originating from the e^* decay process are most likely to be found in the forward hemisphere of the H1 detector, as will be shown again in section 4.3.1.

3.1.3 The cross sections

The description of wide angle bremsstrahlung presented in this section follows ref. [22]. Demanding the scattered electron and photon originating from the process $ep \to ep\gamma$ to be measured in the HERA detectors, i.e. in a polar angle range $1° < \Theta < 179°$ the phase space is restricted to the so called "wide angle bremsstrahlung" regime. This kinematic domain is characterized by the fact that the invariant mass squared $\hat{s}$ of the $e\gamma$-system and $\hat{t}$, the four momentum transfer squared between the in and outgoing electron are very large compared to m_e^2.

Neglecting photon radiation at the hadronic side the cross section can be calculated from the Feynman-diagrams in fig. 3.1. In this figure also the inelastic bremsstrahlung

$$e + p \to e + \gamma + X \tag{3.8}$$

is included, where X denotes an arbitrary hadronic final state. With $X = p$ the limiting case of elastic wide angle bremsstrahlung is retained.

Elastic wide angle bremsstrahlung

The cross section formula for the reaction $ep \to ep\gamma$ cannot simply be taken from QED textbooks like [23] because the proton structure has to be taken into account. Formulas for the fully differential cross section can be found in refs. [24, 25]. Here the approach of Courau and Kessler [26] where the differential cross section is given as a product of photon flux factors and differential cross sections for the virtual Compton effect $\gamma^* + e \to \gamma + e$ is followed. The cross section is written as sum of a magnetic and an electric term

$$\frac{d\sigma}{dk^2 dy dz d\phi} = \frac{d\sigma^M}{dk^2 dy dz d\phi} + \frac{d\sigma^E}{dk^2 dy dz d\phi} \quad , \tag{3.9}$$

where $k^2 = (p - p')^2$ is the mass squared of the virtual photon radiated from the proton. Furthermore

$$y = \frac{e \cdot e'}{e \cdot k} = \frac{1}{2}(1 - \cos\theta_{cms}) \tag{3.10}$$

is connected to the scattering angle $\theta_{\rm cms}$ in the $e\gamma^*$ subsystem and

$$z = \frac{e \cdot k}{e \cdot p} = \frac{\hat{s} + |k^2|}{S - m_p^2} \tag{3.11}$$

(where S is the ep center of mass energy squared) can be interpreted as the fractional momentum of the virtual photon in the proton infinite momentum frame. Finally ϕ is the angle between the $e\gamma$-plane[3] and the proton scattering plane[4]. With these definitions the magnetic and electric cross sections read

$$\frac{d\sigma^M}{dk^2 dy dz d\phi} = \Gamma_M \cdot \left(\frac{d\sigma_t}{dy d\phi} + \epsilon \frac{d\sigma_l}{dy d\phi} + \epsilon \frac{d\sigma_p}{dy d\phi} + \sqrt{2\epsilon(\epsilon+1)} \frac{d\sigma_i}{dy d\phi} \right) \tag{3.12}$$

[3]The $e\gamma$-plane is defined by the outgoing electron e' and photon γ.

[4]This plane is defined by the incoming and outgoing proton.

and

$$\frac{d\sigma^E}{dk^2 dy dz d\phi} = \Gamma_E \cdot \left(\frac{d\sigma_t}{dy d\phi} + \frac{1+\epsilon}{2\epsilon}\frac{d\sigma_l}{dy d\phi} + \frac{d\sigma_p}{dy d\phi} + \sqrt{\frac{2(\epsilon+1)}{\epsilon}}\frac{d\sigma_i}{dy d\phi} \right) \quad . \tag{3.13}$$

Herein Γ_M and Γ_E are given by

$$\Gamma_M = \frac{\alpha G_M^2}{|k^2|\pi z} g_T \quad , \quad \Gamma_E = \frac{\alpha G_E^2 4m_p^2}{|k^2|^2 \pi z} g_L \tag{3.14}$$

with

$$g_L = \frac{(1-z)|k^2| - z^2 m_p^2}{|k^2| + 4m_p^2} \tag{3.15}$$

$$g_T = \frac{(1-z)|k^2| - z^2 m_p^2}{|k^2| + 4m_p^2} + \frac{z^2}{2} \quad . \tag{3.16}$$

The magnetic and electric formfactors $G_M(k^2)$ and $G_E(k^2)$ are only known empirically and are mostly approximated by the so called dipole formula [27], i. e.

$$G_E(k^2) \approx \frac{G_M(k^2)}{2.79} \approx \left(1 + \frac{k^2}{0.71\mathrm{GeV}^2}\right)^{-2} \quad . \tag{3.17}$$

The polarization parameter ϵ is defined by

$$\epsilon = \frac{g_L}{g_T} \quad . \tag{3.18}$$

The virtual Compton cross section formulas come from the Mendez paper [28]. The longitudinal (index l), polarized (p) and interference term (i) vanish with k^2. Neglecting these terms reduces (3.9) to the equivalent photon approximation

$$\frac{d\sigma}{dk^2 dy dz d\phi} = (\Gamma_M + \Gamma_E)\frac{d\sigma_t}{dy d\phi} \quad . \tag{3.19}$$

The sum $(\Gamma_M + \Gamma_E)$ of the two flux factors equals the well known photon flux from a pointlike particle [29] if $G_M = G_E = 1$ is chosen. The Weizsäcker Williams approximation (WWA) neglects the k^2 dependence of the Compton cross sections and integrates over k^2 in the flux factors (3.14). Thus the incoming proton is replaced by a photon beam with a known energy spectrum. For a pointlike particle this spectrum has been calculated for the first time by Kessler [29]. Another interesting review by Budnev et al. can be found in [30]. A handy formula for the photon spectrum radiated by the proton can be found in ref. [31]. This calculation uses the dipole formula for the form factors.

It is important to note that, compared to the flux factor of a pointlike particle, the extremely steep decrease of (3.14) with k^2 results in a very good description of the cross section by the WWA in almost the entire phase space. During the development phase of the WABGEN generator this has been checked numerically by comparing the results of the new generator with a routine utilizing the WWA.

Inelastic wide angle bremsstrahlung

For higher values of $|k^2|$ inelastic processes, where the proton breaks up into a final state X, become more and more likely. These reactions can be calculated in the quark model by replacing the incoming proton by a beam of quarks with momentum fraction ξ of the incoming proton. The virtual photon flux from the quarks can be obtained using the pointlike formula with a quark mass of 300 MeV. The virtual photon four vector k^μ and ξ uniquely determine the invariant mass W of the final hadronic system. For $|k^2| > 5$ GeV^2 and $\xi < 0.99$ (i.e. excluding the elastic peak) one can use standard parton density parameterizations[5].

In order to also describe resonance production, $ep \to e\gamma R$, quasielastic processes with $|k^2| < 5$ GeV^2 and $m_p < W < 1.8$ GeV have to be taken into account. This can be achieved by replacing the sum of the parton densities in the usual way by the proton structure function F_2 from the empirical fits of ref. [33]. The contribution of the continuum with $W > 1.8$ GeV is neglected in this approach.

3.2 Background Processes

The appearance of just an electron and a photon in an event within the H1 detector is not necessarily due to the reaction $ep \to ep\gamma$. Other reactions can lead to the same signature as well. These are classified as being physical or unphysical background. Unphysical background originates from reactions not belonging to ep collisions. These include cosmic radiation, beam halo events and collisons of the accelerated eletrons and protons with residual gas atoms. Physical background is produced by proper ep reactions. In most cases it is not possible to distinguish between physical background faking the investigated reaction and real events. Background processes for wide angle bremsstrahlung are presented in the following sections.

3.2.1 Deep Inelastic Scattering

A major part of the physics investigated at HERA is DIS[6]. Fig. 3.2 shows the accompanying Feynman diagrams in lowest order. These processes allow to measure the internal structure of the proton. On the Born level the incoming electron interacts with a quark by the exchange of a photon/Z^0 boson (Neutral Current/NC) or a W boson (Charged Current/CC). Afterwards the struck quark and the proton remnant form hadronic jets. These jets can contain neutral pions π^0. Due to their short lifetime of $\tau = 0.87 \cdot 10^{-15}$ s they decay within the H1 detector. Approximatly 100% transform into two real photons ($\pi^0 \to \gamma\gamma$). If the angle between these two photons is small enough they are identified as a single electromagnetic cluster in the LAr calorimeter and hence fake a photon. If the scattered electron is also detected and the jet remnant leaves the detector through the beam pipe without being observed the event can be misinterpreted as a WAB candidate.

[5] WABEN then simulates the final state with the help of the JETSET 7.4 routine [32].

[6] Deep Inelastic Scattering

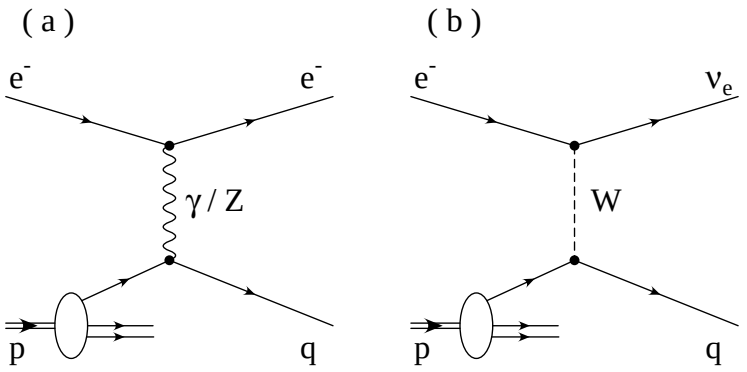

Figure 3.2: Feynman diagrams for deep inelastic scattering. (a) shows the neutral current reaction and (b) the charged current reaction.

3.2.2 Photon Photon Scattering

Fig. 3.3 shows the process of photon photon scattering where both electron and proton emit a quasireal photon along with the subsequent production of a lepton pair l^+l^-. When searching for WAB events the production of a e^+e^- pair via photon photon scattering, i. e.

$$e^-p \rightarrow e^+e^-e^-p$$

has to be considered as possible background source. The spectra of the photon energies have their maximum at low values. Thus the invariant mass of the e^+e^- system is also small. For the misidentification of the e^+e^- pair two conditions have to be fulfilled:

- one of the three outgoing leptons and the proton must leave H1 undetected via the beam pipe and
- one of the two remaining leptons has to be reconstructed without a track.

These conditions would lead to an event topology consistent with wide angle bremsstrahlung. A previous study [18] of this background process has found a probability of 3.3% of finding events of this type[7]. In [18] two electromagnetic clusters were demanded together with less stringent cuts needed for the identification of WAB events. Due to the extreme constraints for the phase space and the demand for a non reconstructed track the background from photon photon scattering is neglected in this study.

3.2.3 Photoproduction

For completeness the process of photoproduction is mentioned here as well. In this reaction a quasireal photon emitted by the incoming electron interacts with one of the constituents of the proton, i. e. a gluon or a quark. Fig. 3.4 shows the typical Feynman diagram. In the search for wide angle bremsstrahlung photoproduction is a background source for the inelastic channel $ep \rightarrow epX$ which can involve jets. Hence it will not be considered here.

[7] This was done for 27.5 GeV electrons and 820 GeV protons.

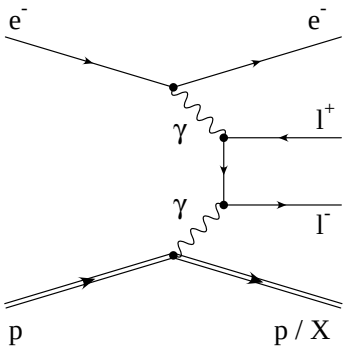

Figure 3.3: Feynman diagram for lepton pair production in photon photon scattering.

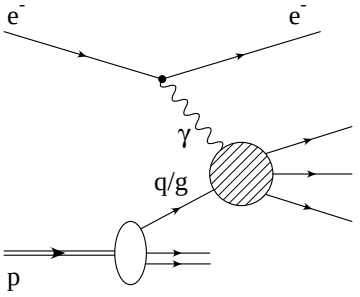

Figure 3.4: Feynman diagram for photoproduction in ep collisions. The hard scattering process is represented by the hatched circle.

3.2.4 e* Production

The production of excited electrons is an interesting non standard model background process for wide angle bremsstrahlung. The existence of excited fermions or quarks f^* would provide clear evidence for fermion substructure because of the possible interpretation as excitations of the ground state. Theories of compositeness have been discussed in the literature quite extensive [34, 35, 36, 37, 38]. Because the dynamics of the compositeness is unknown it is conventional to use the phenomenological model of Hagiwara et al. [39] which has the advantage of maintaining generality in describing f^* production and decay. Although the possible compositeness scale Λ is expected to be in the order of 1 TeV it is possible that the lowest excited states have masses below this value, i. e. a few hundred GeV. Their production at HERA could therefore be feasible.

In the model of Hagiwara et al. exited spin 1/2 fermions f^* are assumed to couple to ordinary fermions f via magnetic transitions[8]. These couplings are described by an effective Lagrangian of the form

$$\mathcal{L}_{eff} = \frac{e}{\Lambda} \sum_{V=\gamma,Z,W^{\pm}} \overline{F}\sigma^{\mu\nu}(c_{Vf^*f} - d_{Vf^*f}\gamma_5) f \partial_\mu V_\nu + h.c.^{9} \tag{3.20}$$

where Λ, the compositeness scale, is independent of of the excited fermion mass. The c_{Vf^*f} and d_{Vf^*f} are the coupling constants at the $f \leftrightarrow f^*$ transition vertex. V labels the corresponding vector boson. Bounds on the couplings c_{Vf^*f} and d_{Vf^*f} are given by low energy experiments. Precise measurements of $g-2$ and theoretical predictions imply $|c_{\gamma f^* f}| = |d_{\gamma f^* f}|$ for compositeness scales less than 10-100 TeV[40, 41, 42]. The absence of electric dipole moments for the electron and the muon requires c_{Vf^*f} and d_{Vf^*f} to have the same phase thus resulting in

$$c_{\gamma f^* f} = d_{\gamma f^* f}.$$

In the case of e^* production via photon exchange eqn. 3.20 becomes

$$\mathcal{L}_{eff} = \frac{e}{\Lambda}\overline{F}\sigma^{\mu\nu}(c_{\gamma e^* e} - d_{\gamma e^* e}\gamma_5) f \partial_\mu V_\nu + h.c. \tag{3.21}$$

Hagiwara et al. choose a specific model [40, 41, 42] for the coupling of SM and excited fermions. The first generation fermions contained in this model can be found in table 3.2. They assume that the excited electron and neutrino form both left and right handed weak isodubletts

$$L^* = \begin{pmatrix} \nu_e^* \\ e^* \end{pmatrix}.$$

The right handed excited states couple to the left handed SM electron doublet

$$l_L = \begin{pmatrix} \nu_e \\ e^- \end{pmatrix}$$

by the SU(2)×U(1) invariant interaction Lagrangian

[8] Excitations of spin 3/2 excited states are discussed in [36], but will not be considered here.

[9] h.c. stands for the hermitian conjugate of the first term.

	SM fermions	Excited fermions
Leptons	$\begin{pmatrix}\nu_e\\ e^-\end{pmatrix}_L \quad e^-_R$	$\begin{pmatrix}\nu_e^*\\ e^*\end{pmatrix}_L \quad \begin{pmatrix}\nu_e^*\\ e^*\end{pmatrix}_R$
Quarks	$\begin{pmatrix}u\\ d\end{pmatrix}_L \quad u_R \quad d_R$	$\begin{pmatrix}u^*\\ d^*\end{pmatrix}_L \quad \begin{pmatrix}u^*\\ d^*\end{pmatrix}_R$

Table 3.2: First generation fermions in the model choosen by Hagiwara et al.

$$\mathcal{L} = \frac{gf}{\Lambda}\overline{L}\sigma^{\mu\nu}\frac{\vec{\tau}}{2}l_L\partial_\mu\vec{W}_\nu + \frac{g'f'}{\Lambda}\overline{L}\sigma^{\mu\nu}Yl_L\partial_\mu B_\nu + h.c. \tag{3.22}$$

Here g and g' are the standard model SU(2) and U(1) coupling constants fulfilling $e = g\sin\theta_W = g'\cos\theta_W$, where θ_W is the Weinberg angle. $\vec{\tau}$ denotes the Pauli matrices and $Y = -1/2$ the hypercharge. $\vec{W}_\nu$ and B_ν describe the SU(2) and U(1) gauge fields respectively. In this model all coupling constants c and d from eqn. 3.20 fulfil $c_{Vf^*f} = d_{Vf^*f}$. For the production of excited electrons $c_{\gamma e^* e}$ can be written as

$$c_{\gamma e^* e} = -\frac{1}{4}(f + f').$$

Since all other quantities are known the cross section for e^* production can be described by a single free parameter, e. g. c/Λ or f/Λ.

In ep collisions single excited electrons e^* could be produced via t-channel γ/Z^0 boson exchange depicted in Fig.3.5. The cross section for e^* production via photon exchange strongly rises for small Q^2 [10]. Hence the Z^0 contribution is negligible and will not be considered here. According to the value of the exchanged four momentum squared the process is called elastic, quasielastic or inelastic. In the elastic case, i. e. $Q^2 \approx 0\,\mathrm{GeV}^2$, the proton remains intact. It leaves the detector by the beampipe without being observed.

The elastic and quasielastic reactions compete with each other in the quasielastic region which extends to values of $Q^2 \lesssim 5\,\mathrm{GeV}^2$. As a result of the larger value of Q^2 in the quasielastic case the proton can be excited and form a resonance state (See table 3.1). Again it leaves through the beampipe without being detected. For the determination of the cross section special parametrizations of the structure functions F_1 and F_2 have to be used. These average over the different resonance states. The inelastic domain starts at $Q^2 > 5\,\mathrm{GeV}^2$. Now a quark can be scattered off the proton and form hadronic jets.

The e* production cross sections

In this section the cross sections for the elastic and quasielastic/inelastic case will be presented without taking into account the Z^0 exchange.

Elastic case ($e + p \to e^* + p$)

The elastic part of the cross section reads

[10] Here Q^2 is defined in the same way as k^2 in the previous sections of this chapter, i. e. it is the mass squared of the virtual photon exchanged by the electron and the photon.

$$\frac{d\sigma}{dQ^2} = \frac{\pi\alpha^2}{\Lambda^2}\frac{|c_{\gamma e^* e}|^2 + |d_{\gamma e^* e}|^2}{(s-m_p^2)^2 Q^2} \cdot \left\{ G_M^2(Q^2)(2m_{e^*}^2 - Q^2)(m_{e^*}^2 + Q^2) + \frac{G_E^2(Q^2) + \frac{Q^2}{4m_p^2} G_M^2(Q^2)}{1 + \frac{Q^2}{4m_p^2}} \cdot \left[4(s-m_p^2)^2 - (m_{e^*}^2 + Q^2)(4s - Q^2 - 4m_p^2 + \frac{4m_{e^*}^2 m_p^2}{Q^2}) \right] \right\}.$$

G_E and G_M are the electric and magnetic form factors of the proton obtained by a dipole fit and given by eqn. 3.17.

Quasielastic and inelastic case $(e + p \to e^* + X)$

$$\frac{d\sigma}{dx dQ^2} = \frac{2\pi\alpha^2}{\Lambda^2} \cdot \frac{|c_{\gamma e^* e}|^2 + |d_{\gamma e^* e}|^2}{(s-m_p^2)^2 x^2 Q^2} \cdot F_2(x,Q^2) \cdot \left\{ m_{e^*}^2(m_{e^*}^2 + Q^2)\left(\frac{1}{x} - \frac{2xm_p^2}{Q^2}\right) + 2x(s-m_p^2)^2 - 2(m_{e^*}^2 + Q^2)(s-m_p^2) \right\}$$

Here the structure function F_2 can be written as

$$F_2(x,Q^2) = \sum_{q=u,d,s,\ldots} Q_q^2 \cdot \left\{ xq(x,Q^2) + \overline{q}(x,Q^2) \right\}.$$

where the summation is done for the different quark flavours.

Integrated cross section

Fig.3.6 shows the integrated cross section for the production of excited electrons at HERA using the model of Hagiwara et al. For completeness the ν_e^* cross section has been included as well. Due to the fact that excited neutrinos can only be produced via W boson exchange the cross section is reduced by roughly one order of magnitude compared with the one for e^*. Hence a search for excited electrons is much more promising than a search for excited neutrinos. In Fig.3.6 initial state radiation has been taken into account along with the following parameters: $f = f' = 1$, $\Lambda = 1\,\text{TeV}$ and $\alpha^{-1} = 128$. For $Q^2 > 4\,\text{GeV}^2$ the parton distribution functions of MRS D$^-$[43] have been used and for the quasielastic domain the structure functions obtained by Brasse et al. [33]. The e^* production cross section separated for the three phase space regions is shown in Fig.3.7. The elastic process is expected to dominate accounting for approximately 50% of the cross section due to t-channel enhancement. The absolute value of the cross section completely depends on the values of f/Λ and f'/Λ because it is proportional to the coupling constant squared, i. e.

$$\sigma(ep \to e^* X) \sim \frac{c_{\gamma e^* e}^2}{\Lambda^2} \sim \frac{(f+f')^2}{\Lambda^2}.$$

It has to be noted that the value of $1\,\mathrm{TeV}^{-1}$ for f/Λ and f'/Λ is arbitrary.
The total cross section σ_{tot} is given by

$$\sigma(ep \to e^*X \to e\gamma X) = \sigma(ep \to e^*X) \cdot BR(e^* \to e\gamma)$$

where $\sigma(ep \to e^*X)$ is one of the previous production cross sections. The branching ratio BR is defined by the ratio of the partial and the total decay width. For the $e\gamma$-decay mode it reads

$$BR(e^* \to e\gamma) = \frac{\Gamma(e^* \to e\gamma)}{\Gamma_{tot}}. \tag{3.23}$$

Γ_{tot} is the total decay with defined by

$$\Gamma_{tot} = \Gamma(e^* \to e\gamma) + \Gamma(e^* \to eZ) + \Gamma(e^* \to \nu W). \tag{3.24}$$

3.2.5 Decay of excited electrons

In principle the decay of excited electrons is possible via the three channels

$$\begin{aligned} e^* &\to e\gamma \\ e^* &\to eZ \\ e^* &\to \nu_e W\,. \end{aligned}$$

The decay widths are given by [44, 45]

$$\Gamma(l^* \to lV) = c^2_{Vl^*l}\alpha\frac{M^3_{L^*}}{\Lambda^2}\left(1 - \frac{M^2_V}{M^2_{L^*}}\right)\left(1 + \frac{M^2_V}{2M^2_{L^*}}\right). \tag{3.25}$$

For the reaction $ep \to e^*X$ one gets

$$\Gamma(e^* \to e\gamma) = c^2_{\gamma e^* e}\alpha\frac{M^3_{e^*}}{\Lambda^2}. \tag{3.26}$$

because the photon mass is zero. Fig.3.8 shows the corresponding branching ratios for e^* masses up to 250 GeV assuming $f = f' = 1$. The decay into Z- and W-bosons is only possible if m_{e^*} is sufficiently above the gauge boson masses. For e^* masses of up to $\sim$120 GeV the decay into an electron and a photon is the predominant one. Above this value the $e\gamma$-branching ratio is still greater than 30%. For $f = -f' = 1$ excited electrons do not couple to photons. Thus the branching ratio is zero, independent of the e^* mass.

In the center-of-mass system of the excited electron the angular distribution of the outgoing electron is decribed by [46]

$$\frac{1}{\Gamma}\frac{d\Gamma}{d\cos\theta^*} \sim \frac{1 + \cos\theta^*}{2}.$$

constraining the kinematics of the process

$$e\gamma \to e^* \to e\gamma.$$

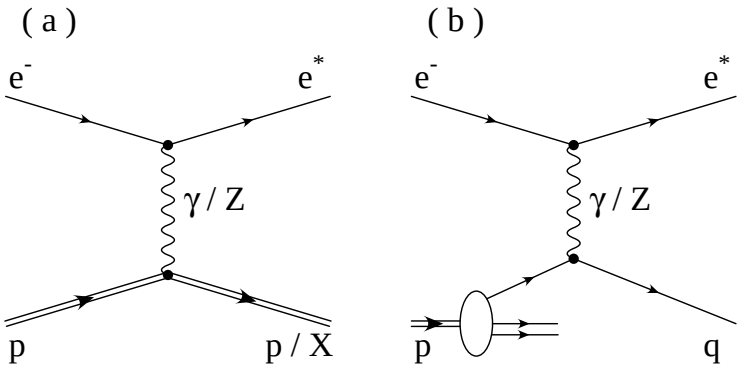

Figure 3.5: Feynman diagrams for e^* production. (a) shows the elastic and (b) the inelastic case.

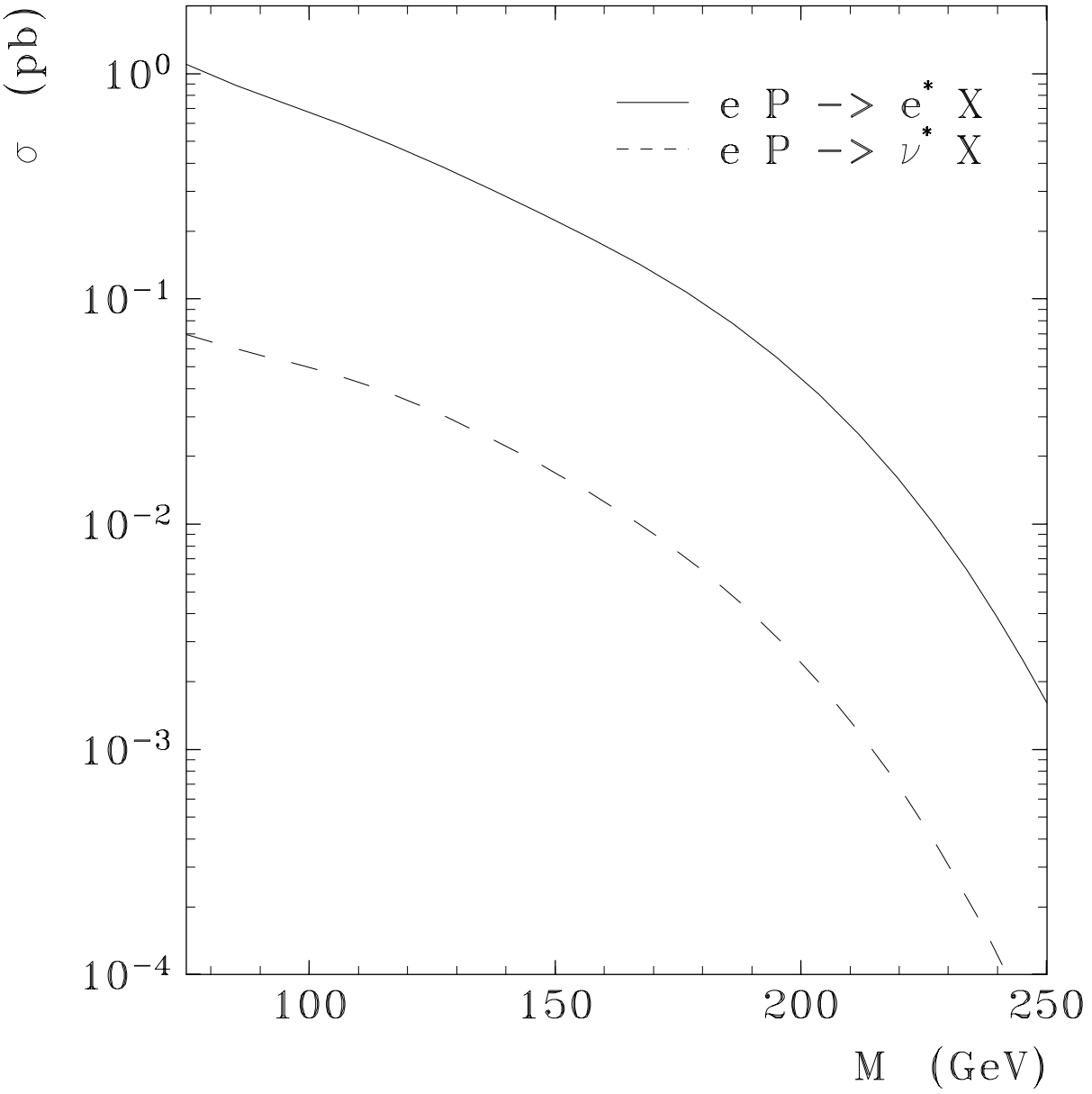

Figure 3.6: Total production cross section for e^* and ν_e^* at HERA. The proton momentum was set to be 820 GeV.

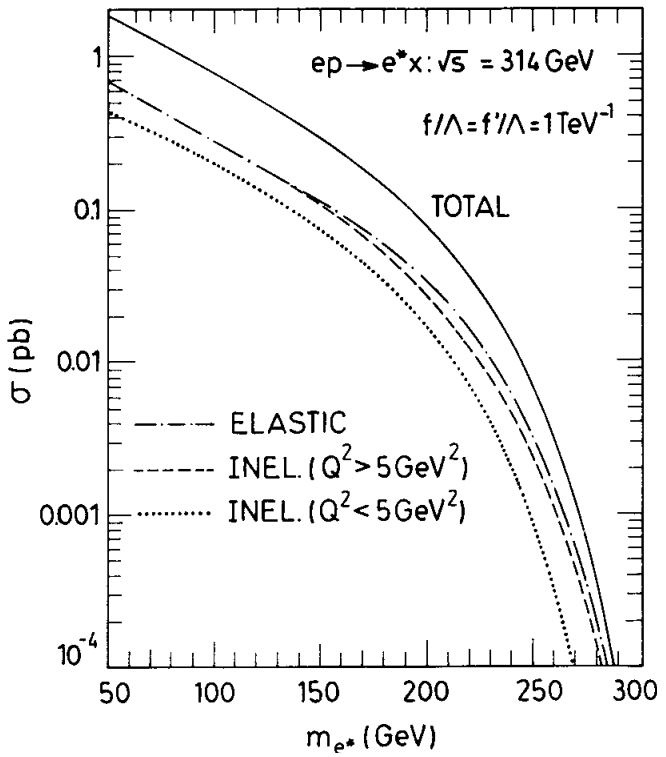

Figure 3.7: Total e^* production cross section for $f/\Lambda = f'/\Lambda = 1\,\mathrm{TeV}^{-1}$. Elastic (dash-dotted line), quasielastic (dotted line) and inelastic (dashed) contribution are shown seperately.

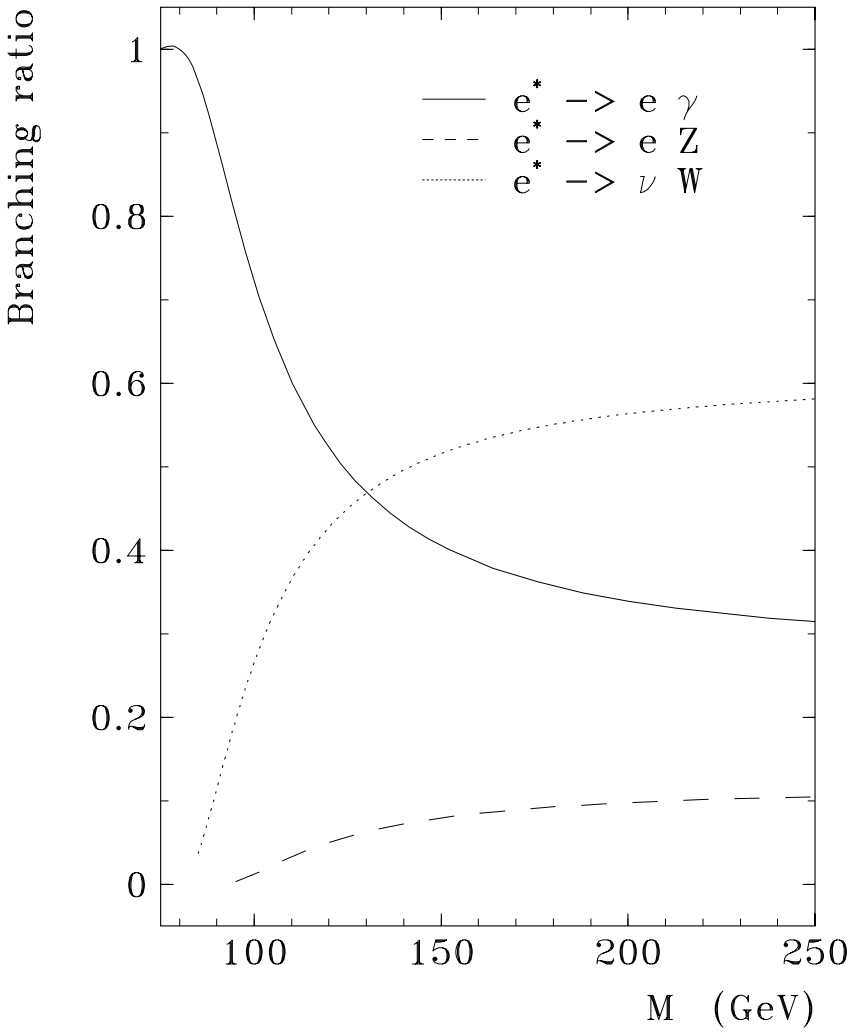

Figure 3.8: Branching ratio BR of excited electrons in different decay channels.

Chapter 4

Event generators

For the investigation of new physics one has to compare the measured data with distributions obtained from event generators in order to check for deviations from the standard model. These programmes compute four-vectors of particles originating from possible physics processes. The aim is to describe the real reactions as accurate as possible. Therefore the differential cross section of the process has to be integrated with high precision. The next step is the generation of randomly distributed points in the phase space acording to its density using a random number generator. After the events have been generated their behaviour in the detector has to be simulated. This is done by means of the GEANT software package [47]. It describes the passage of the generated particles through the detector material. Now the Monte Carlo events are comparable with real data. The last step is the reconstruction. Both real and Monte Carlo data use the same reconstruction software. These programmes transform the information from the detector to physical objects, e. g. hits from the central tracking system to particle tracks with a certain momentum.

4.1 The WABGEN package

In order to determine the expected number of events originating from wide angle bremsstrahlung the event generator WABGEN [22] was used. It allows to generate WAB events in all three kinematic domains, i. e. elastic, quasielastic and inelastic. The elastic process $ep \rightarrow ep\gamma$ is simulated according to the eqns. 3.9, 3.12 and 3.13 of section 3.1.3. The simulation of inelastic events follows the description of inelastic wide angle bremsstrahlung in the same section. In the resonance region WABGEN applies a many body phase space model for the simulation of the final state. The decay into charged pions is simulated according to [48]. Their number follows a Poisson distribution.

The elastic and inelastic cross section is numerically calculated using the Monte Carlo package BASES [49]. The package SPRING, which is included in the same distribution then generates weight 1 events in the selected region of phase space. The program calculates from the generated z and k^2 the four momentum of the virtual photon. After generating the kinematic variables in the photon electron CMS, the four momenta of all particles are computed in the HERA laboratory system and stored in H1 banks. In order to check the transformations the four-momentum conservation is controlled numerically

Year	Channel	σ [pb]	$\mathcal{L}$ [pb^{-1}]	Proton momentum	Lepton type
'95-'97	elastic	15.22	328.28	820 GeV	e^+
	quasielastic	9.04	552.52		
	inelastic	15.75	317.29		
'99	elastic	15.92	313.89	920 GeV	e^-
	quasielastic	9.38	532.94		
	inelastic	16.66	300.03		

Table 4.1: Cross sections and luminosities of generated WABGEN events. In each case 4999 events have been generated.

for each event.

For every kinematic domain 4999 events were generated in order to minimize the statistical error. The parameters of the generation were the following:

- electron momentum -27.5 GeV, proton momentum 820 GeV('95-'97) or 920 GeV('99)
- initial state radiation disabled[1]
- energy of outgoing electron and γ between 1 GeV and 10 TeV [2]
- invariant mass in $e\gamma$ subsystem between 0 GeV and 10 TeV [2]
- transverse momentum p_t for outgoing electron and γ between 0 GeV and 10 TeV [2]
- polar angle for outgoing electron and γ between 2° and 155°
- acoplanarity angle between 0° and 360°.

Table 4.1 shows the corresponding cross sections and luminosities. All the 14997 e^+ events were simulated and then reconstructed for the run periods '95, '96 and '97 using the corresponding noise files of the calorimeters. For the first data taking period in '99 when e^- data were collected no noisefiles existed yet. Therefore the noisefiles describing the '98 running conditions were used to reconstruct the generated events.

4.2 The DIS Monte Carlo DJANGO

In order to determine the background originating from DIS two simulated and reconstructed monte carlo files were used. In both cases the generator was DJANGO6.2 [50]. Table 4.2 shows the most relevant parameters of the generation[3]. Again for the '99 run period the files were simulated using the '98 run conditions.

[1] This feature is implemented in the Monto Carlo generator but not tested.

[2] Since WABGEN requires an upper bound for the energy and the transverse momentum of the outgoing electron as well as the invariant mass in the $e\gamma$ subsystem these values were set to be sufficiently high.

[3] These files were choosen because they have already been available within the H1 collaboration and best fitted the requirred parameters.

Run period	'97	'99
Lepton type	e^+	e^-
Proton momentum [GeV]	820	920
minimum Q^2 [GeV^2]	90	60
Events	99999	99968
Cross section [pb]	6319.81	7790.23
Luminosity [pb^{-1}]	15.82	12.83

Table 4.2: Main parameters of the DJANGO DIS files.

4.3 The e* event generator COMPOS

For the generation of e^* event samples the excited fermion event generator COMPOS is available within the H1 collaboration. A detailed description of COMPOS can be found in [51, 52]. It is based on the model of Hagiwara et al. Using COMPOS it is possible to study the production and decay of excited electrons at HERA. Table 4.3 shows the production cross sections of excited electrons with masses between 50 GeV and 250 GeV. The numbers were obtained by an integration with the following parameters:

- COMPOS Version 1.5
- positron momentum -27.5 GeV, proton momentum 820 GeV or 920 GeV
- no polarisation of incident positrons
- bremsstrahlung of incident positrons enabled
- parton showers in the final state enabled
- parametrization of Brasse et al. [33] for ($Q^2 < 4\,\mathrm{GeV}^2$) with R=0.18
- parton distribution function of MRS H [43]for ($Q^2 > 4\,\mathrm{GeV}^2$)
- u,d,s,c quarks enabled
- no intrinsic transverse momentum of the quarks
- elastic, quasielastic and inelastic e^* production
- excited electrons have constant mass
- $\Lambda = 1\,\mathrm{TeV}$, $f = f' = 1$, $\mathrm{M}_W = 80.6\,\mathrm{GeV}$, $\mathrm{M}_Z = 91.2\,\mathrm{GeV}$
- $\alpha^{-1} = 128$, $\sin^2\theta_W = 0.229$
- costant particle masses in JETSET
- no decay of particles with lifetimes $\tau < 0.8 \cdot 10^{-8}\,\mathrm{s}$ (H1 standard)

	$\sigma(ep \to e^*X)$ [pb]	
M_{e^*}[GeV]	$p_p = 820\,\text{GeV}$, $l = e^+$	$p_p = 920\,\text{GeV}$, $l = e^-$
50	1.669	1.875
75	1.065	1.219
100	0.675	0.783
150	0.236	0.290
200	0.053	0.077
250	0.002	0.007

Table 4.3: Cross sections for e^* production at HERA from the Hagiwara model. The accuracy of the integration is 1%. p_p denotes the proton momentum and l the lepton type.

- momentum fraction of quarks inside the proton $> 10^{-3}$
- momentun fraction z of the photon emitted by the incoming electron in the range of $0.0001 < z < 0.9999$ or $z = 0$
- accuracy of the integration 1%.

The fine structure constant α was set to $\alpha^{-1} = 128$ to take into account its running. All events are weighted according to this value of the coupling constant.

4.3.1 Distributions of e* events

In the case of elastic e^* production the decay channel $e^* \to e\gamma$ has a clear signature in the detector. In most cases the proton remains undetected. Because of its small scattering angle it leaves H1 through the beampipe. The electron and photon can be identified easily. All one has to look for are two isolated electromagnetic clusters. If the invariant mass of the $e\gamma$ system is large enough both clusters lie in the Liquid Argon calorimeter. In addition there is no or little hadronic activity in the event. Fig.4.1 shows an e^* event generated by COMPOS after simulation and reconstruction with H1 standard software. The e^* mass was set to be 150 GeV. Both electromagnetic clusters are located in the LAr calorimeter due to the boost into the forward direction. Conservation of the transverse momentum forces both particles to have a separation of 180° in the radial plane. Fig.4.2 shows the energy distribution of electrons and photons originating from e^* events generated by COMPOS. This and the following plots represent the parton level, i. e. no simulation and reconstruction was performed. Events were generated for e^* masses of 75 GeV and 200 GeV. For the high e^* mass the photon and electron energy can reach values of up to 500 GeV. Fig.4.3 shows the sum of E_e and E_γ and Fig.4.4 the transverse energy $E_{t_{e/\gamma}} = E_{e/\gamma} \cdot \sin\theta_{e/\gamma}$. The difference of the azimuthal angles $\Delta\phi = \phi_e - \phi_\gamma$ is plotted in Fig.4.5. The distribution strongly peaks at 180° because of momentum conservation of the transverse component.

The polar angles θ_e and θ_γ are depicted in Fig. 4.6. For the high e^* mass both distributions are shifted to smaller values of θ. This behaviour represents the fact that electron

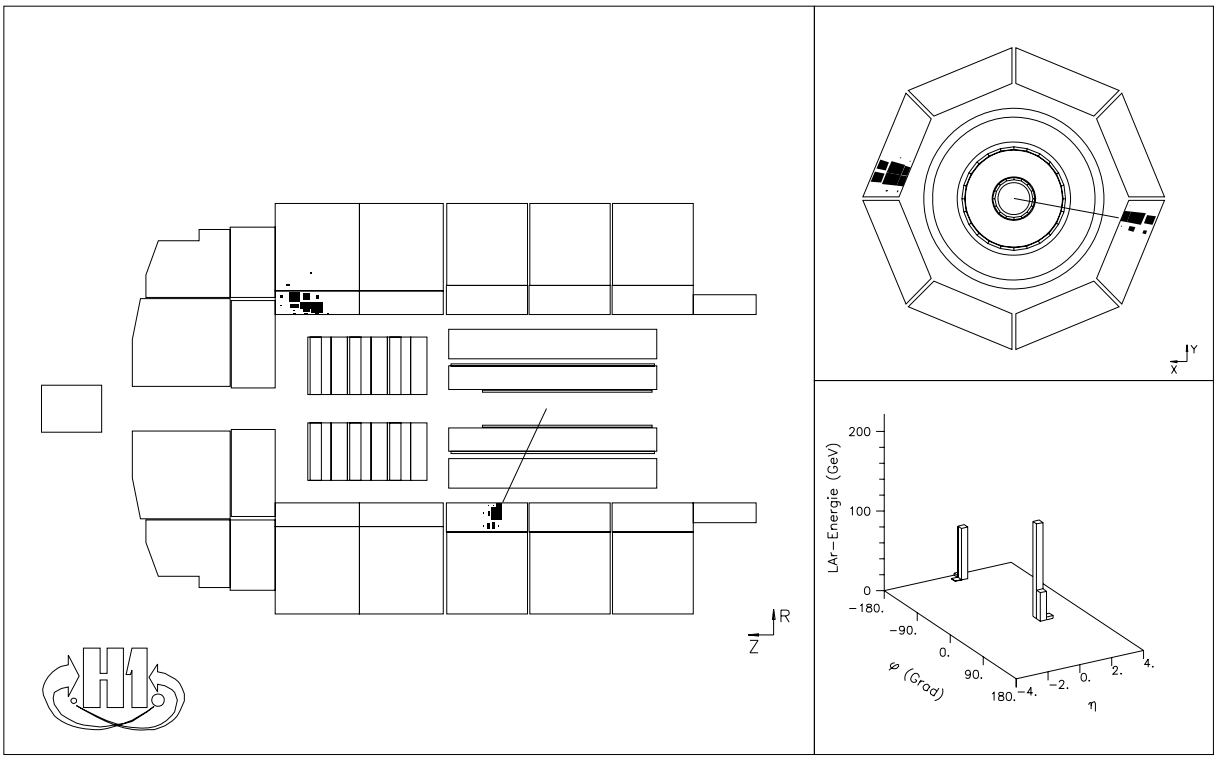

Figure 4.1: An e^* event generated by COMPOS after simulation and reconstruction. The mass of the excited electron is 150 GeV.

and photon are more and more boosted into the forward direction as m_{e^*} increases. Even for $m_{e^*} = 75\,\mathrm{GeV}$ only a small fraction of the electrons can be found above 150°. Cutting there one only accepts clusters from the LAr calorimter disregarding the backward calorimeter (SPACAL).

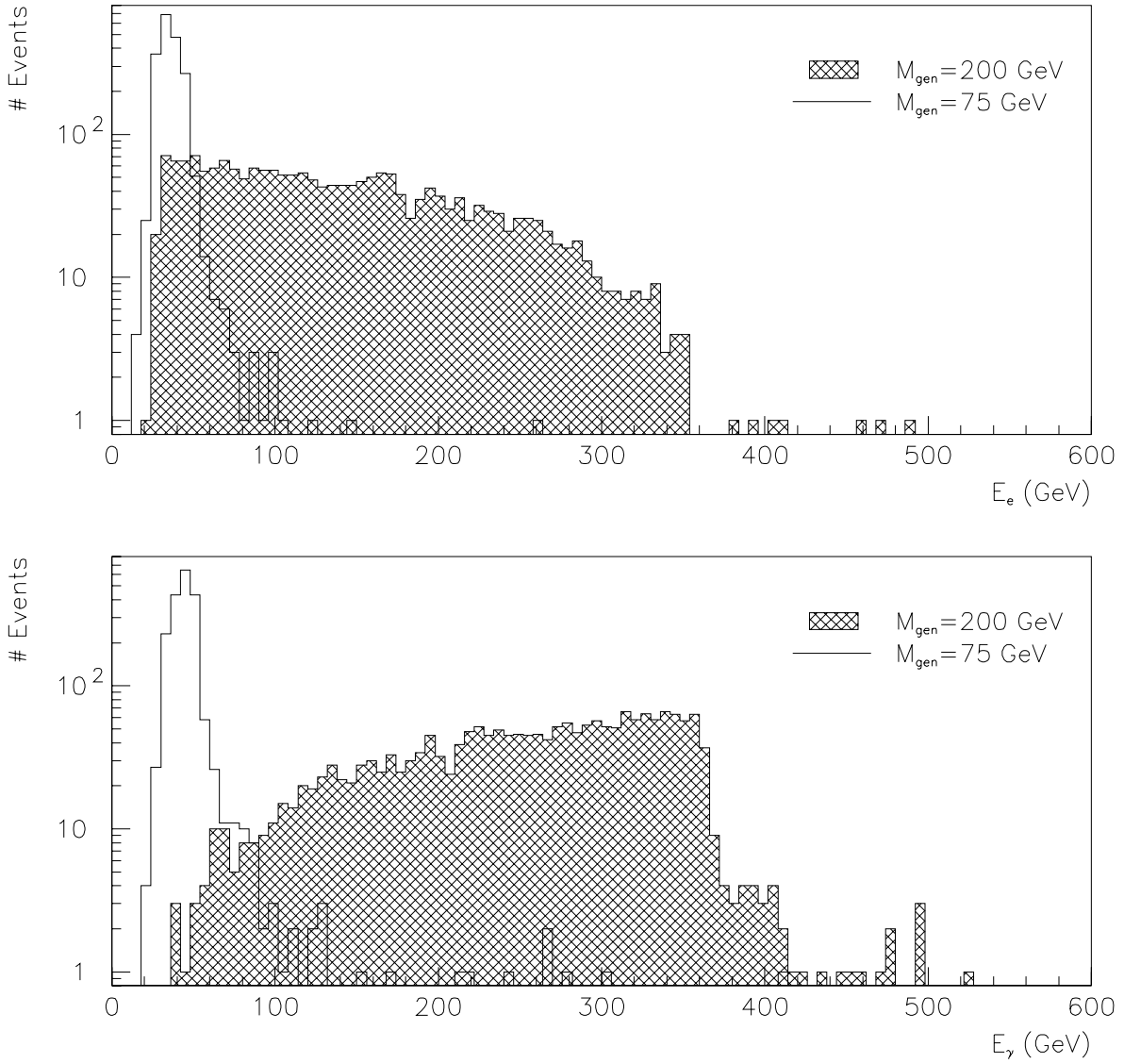

Figure 4.2: Energy distribution for E_e and E_γ.

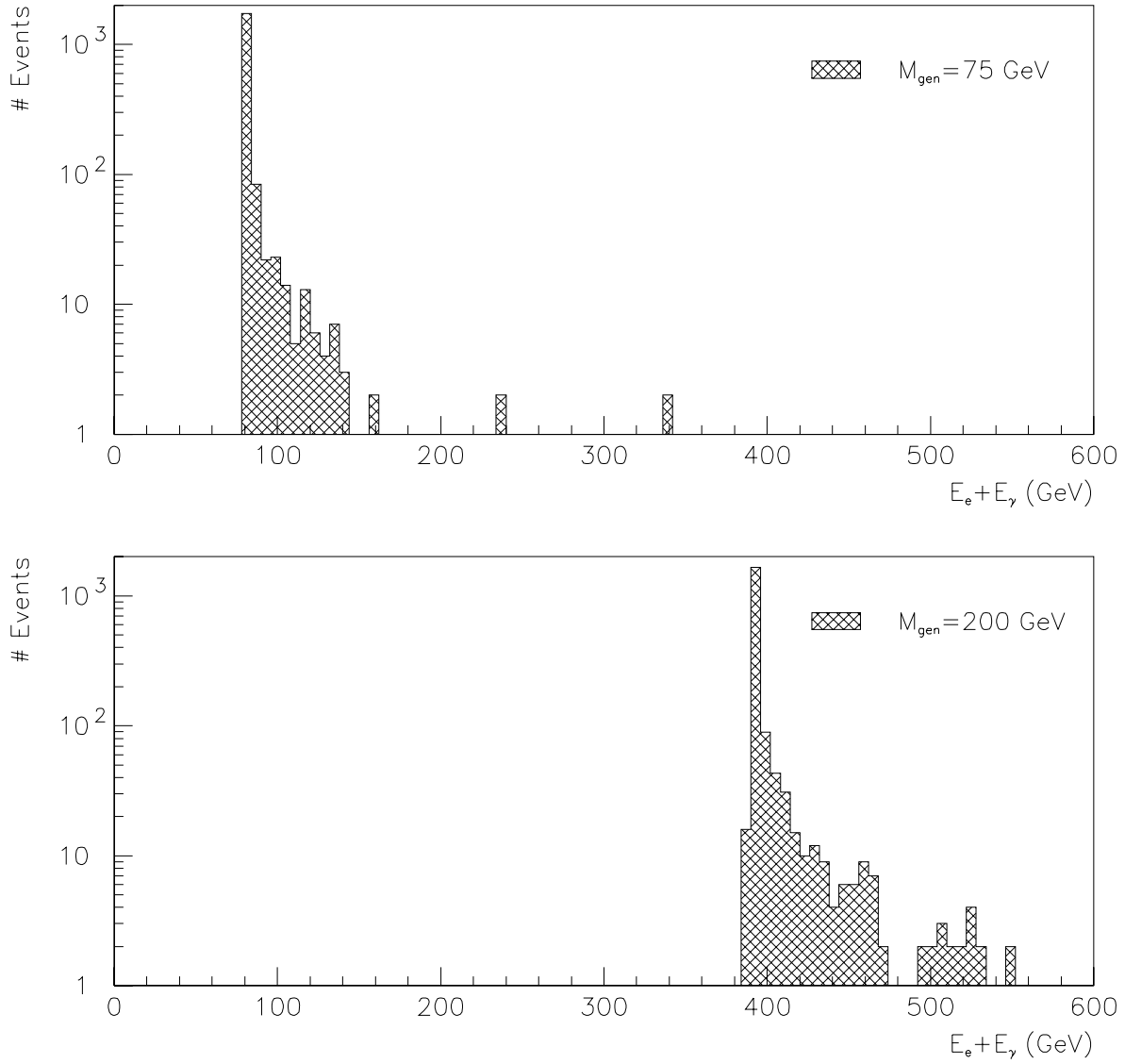

Figure 4.3: Energy distribution for the sum $E_e + E_\gamma$.

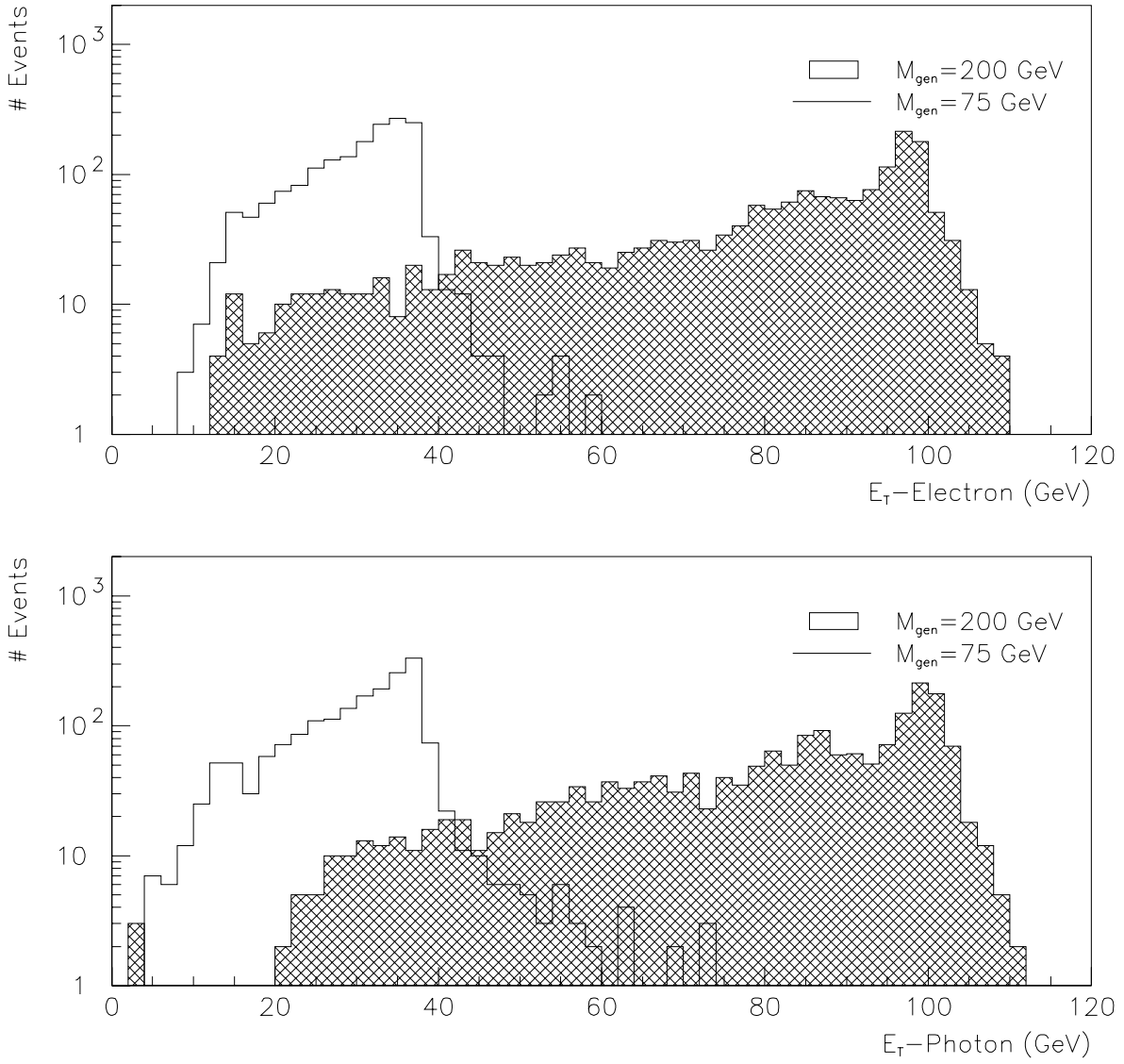

Figure 4.4: Distribution of the transverse energy $E_{t,e}$ and $E_{t,\gamma}$.

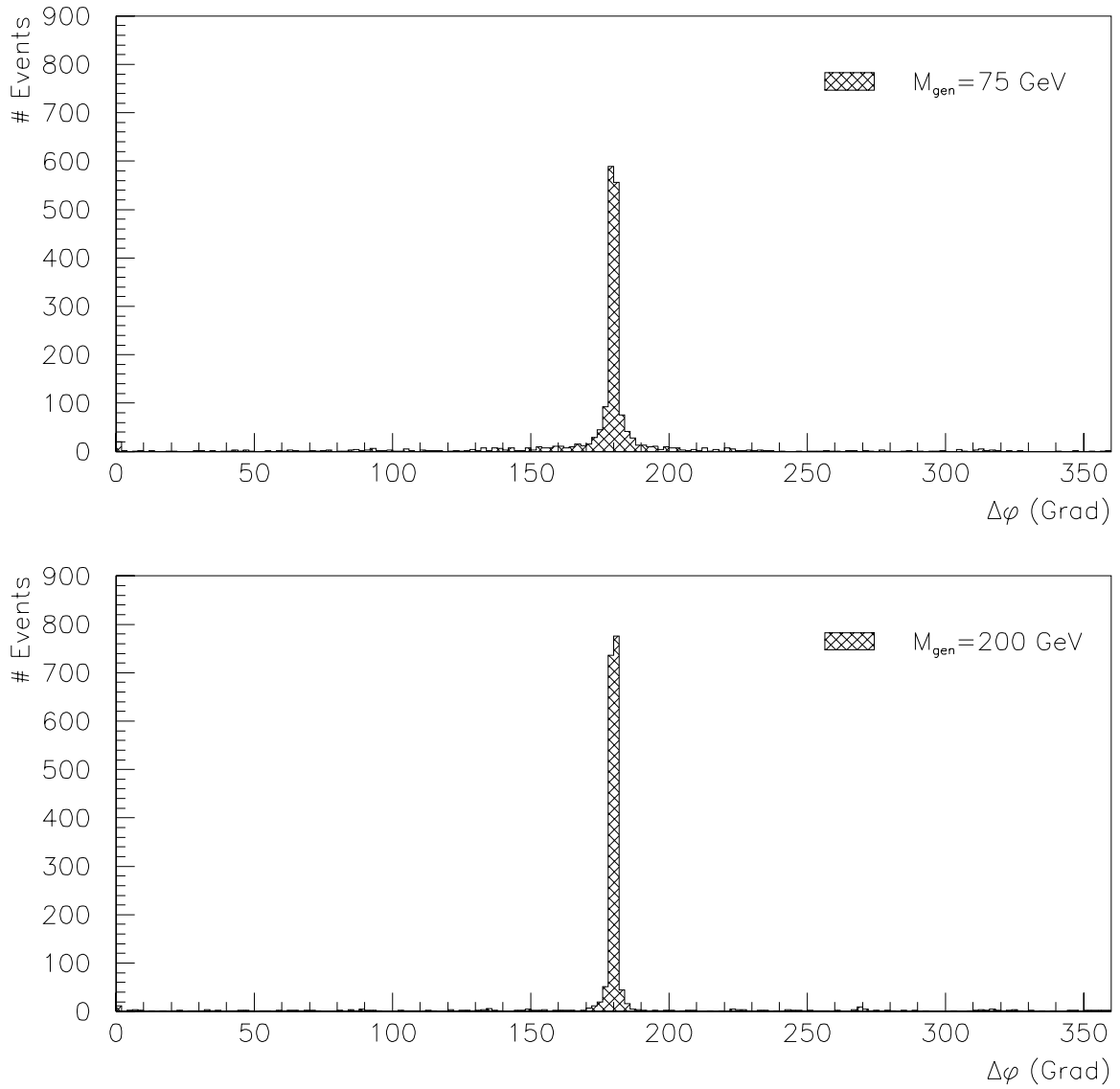

Figure 4.5: Angular distribution $\Delta\phi = \phi_e - \phi_\gamma$ of electrons and photons in the decay channel $e^* \to e\gamma$.

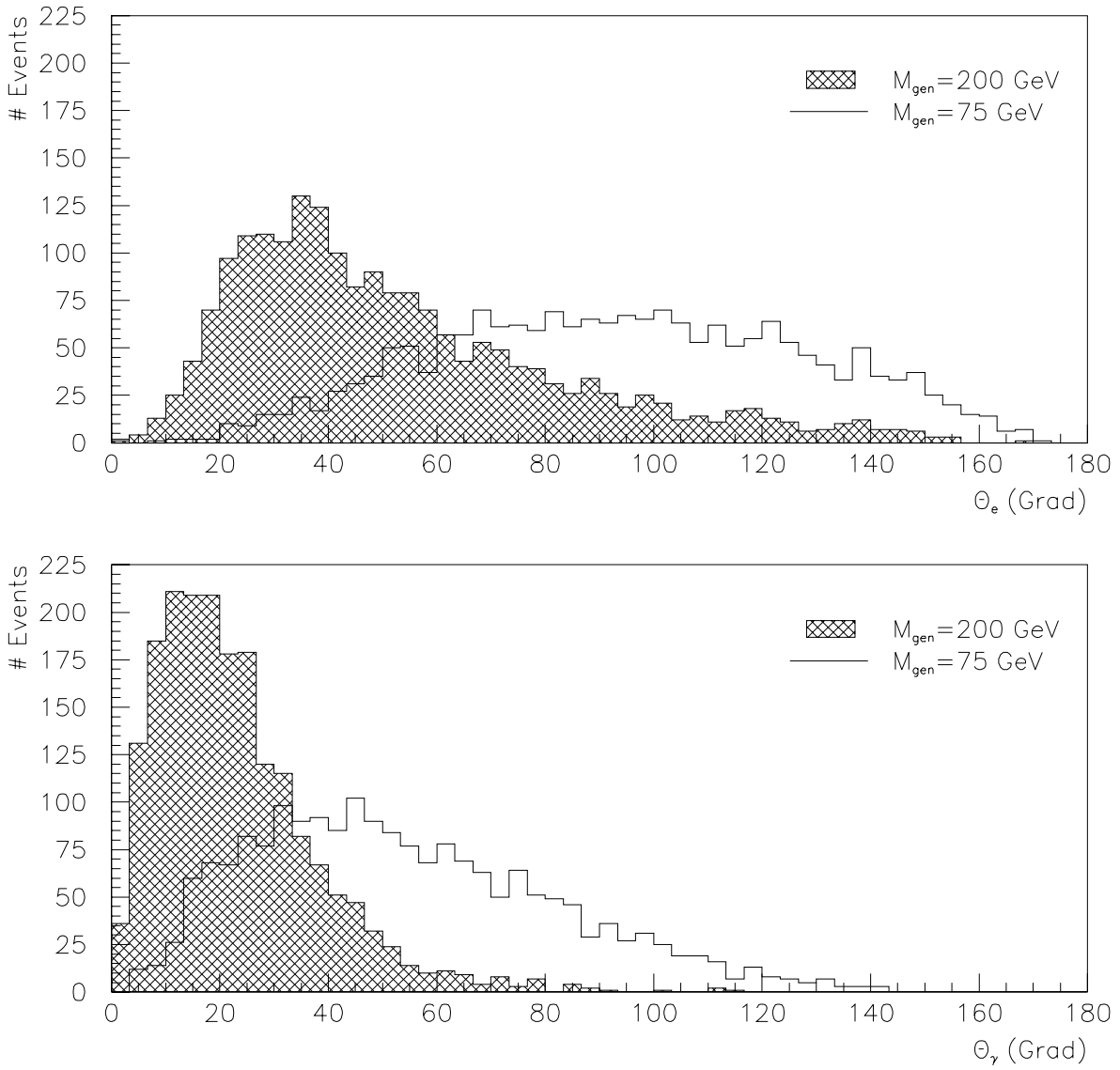

Figure 4.6: Angular distribution θ_e and θ_γ of electrons and photons.

Chapter 5

Data analysis

5.1 Determination of the luminosity

The analysis described in the following sections is based on H1 data collected in the run periods '95-'97 and '99. For 1997 and 1999 two neutral current preselections [53] were used in order to speed up the data access. For 1995 and 1996 the complete data were used for the analysis. In order to determine the integrated luminosity the two selection scenarios of table 5.1 and table 5.2 were applied to the data. The resulting plots can be seen in fig. 5.1. All curves show a smooth course without discontinuities. The event numbers for the lower curves are much smaller than for the upper ones. This is due to the fact that a photon is demanded in the detector in addition to an electron. The integrated luminosities obtained from fig. 5.1 are listed in table 5.3.

5.2 The selection cuts

For the analysis of elastic wide angle bremsstrahlung one has to select events with two electromagnetic clusters in the LAr calorimeter. One of them must have a track pointing towards it. This one is identified as the electron cluster. The second cluster must have no track attached to it because the causing photon is neutral. Appart from the e.m. clusters there should be no or just little energy deposited in the calorimeters. Events originating from the WAB process represent a subsample of neutral current events. The selection cuts are listed in table 5.4 and subsequently explained in more detail.

$-29\,\mathrm{cm} < z_{vertex} < 31\,\mathrm{cm}$
$38\,\mathrm{GeV} < \sum(E - p_z) < 70\,\mathrm{GeV}$
$10^\circ < \theta_e < 150^\circ$
$p_{t,miss} < 20\,\mathrm{GeV}$
$E_e > 15\,\mathrm{GeV}$

Table 5.1: 'Soft' selection cuts for the determination of the luminosity.

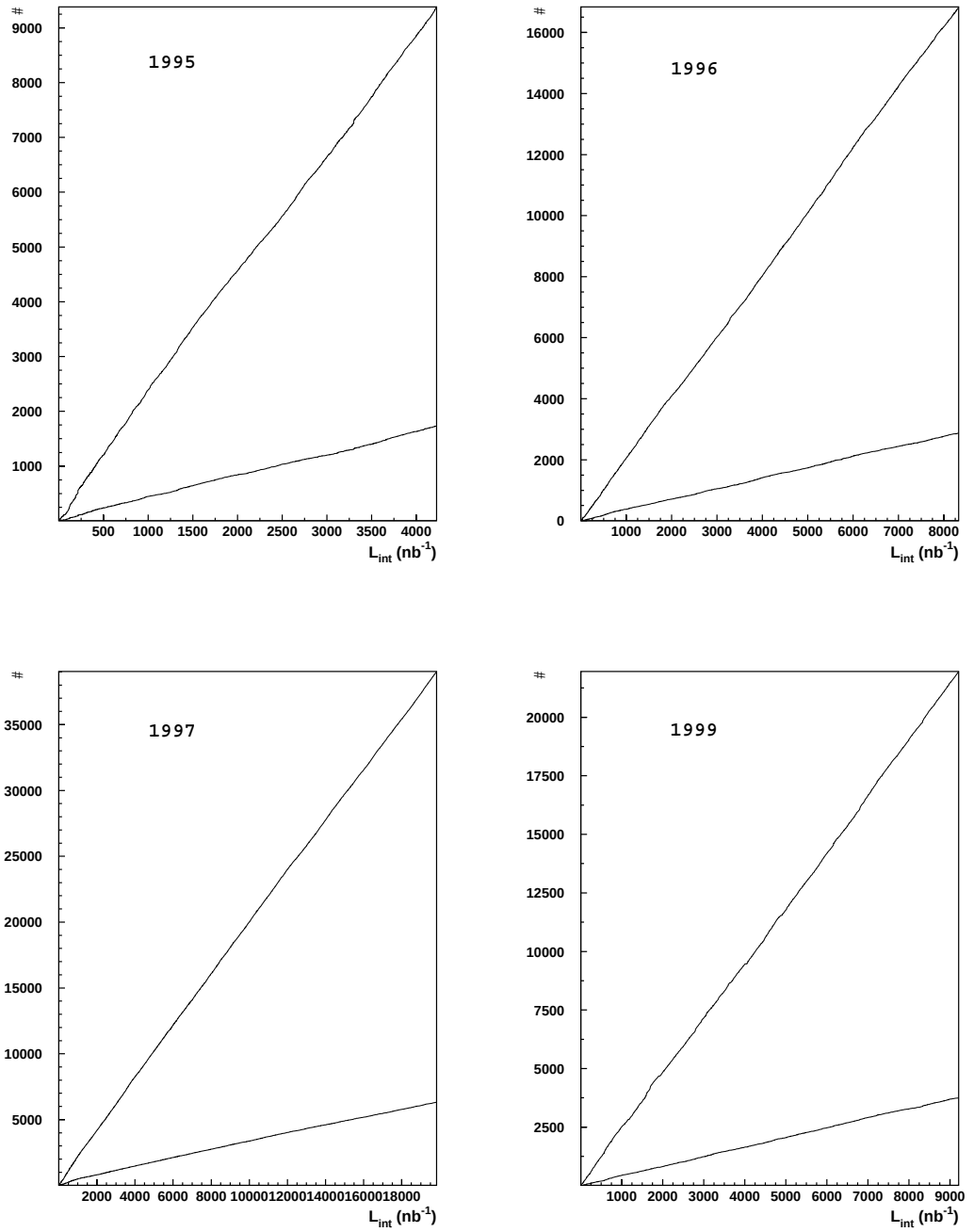

Figure 5.1: Luminosity plots for the different years. The accumulated events are plotted against the integrated Luminosity $\mathcal{L}_{int}$. The upper curves correspond to the selection cuts of table 5.1 whereas the lower curves belong to the selection criterions of table 5.2.

$-29\,\mathrm{cm} < z_{vertex} < 31\,\mathrm{cm}$
$38\,\mathrm{GeV} < \sum(E - p_z) < 70\,\mathrm{GeV}$
$10^\circ < \theta_e < 150^\circ$
$6^\circ < \theta_\gamma < 150^\circ$
$E_e > 2\,\mathrm{GeV}$
$E_\gamma > 2\,\mathrm{GeV}$
$E_e + E_\gamma > 18\,\mathrm{GeV}$

Table 5.2: 'Hard' selection cuts for the luminosity check.

Year	$\mathcal{L}\,[\mathrm{pb}^{-1}]$	CM-energy	Lepton type
1995	4.23		
1996	8.33	300 GeV	e^+
1997	19.84		
$\sum$'95-'97	32.40		
1999	9.22	318 GeV	e^-

Table 5.3: Analysed data, split up by years.

1) Run quality good or medium
The runquality depends on the detector components being in operation during the run. Within H1 it is classified as good, medium or poor. Only events collected during good and medium runs are accepted for futher analysis.

2) event contained in class 9, 12 or 14

- Class 9: neutral current, high Q^2 (NCHQSQ)
- Class 12: elastic QED Compton events (QEDCOM)
- Class 14: special signatures, no muon (SPSNMU)

These three classes contain QED Compton events as well as e^* candidates with high invariant mass.

3) HV bits for CJC1, CJC2, LAr and luminosity system
The power supply had to be in operation for the high voltage of CJC1, CJC2, LAr and the luminosity system.

4) $25\,\mathrm{GeV} < \sum(E - p_z) < 70\,\mathrm{GeV}$
The sum of $E - p_z$ over the entire detector has to be in the range from 25 GeV to 70 GeV. Breaking $E - p_z$ up into a part which is detected and one which is not gives

$$E_{total} - p_{z,total} = E_{vis} - p_{z,vis} + E_{nvis} - p_{z,nvis}\,.$$

Assuming $E_{vis} - p_{z,vis} = 0$, i. e. the undetected particles are highly relativistic or massless and have no transverse momentum, $E_{vis} - p_{z,vis}$ is a conserved quantity. It peaks around $2E_e = 55\,\mathrm{GeV}$. Due to the limited detector resolution the upper limit was set to be

1. Run quality good or medium
2. event contained in class 9,12 or 14
3. HV bits for CJC1, CJC2, LAr and luminosity system
4. $25\,\text{GeV} < \sum(E - p_z) < 70\,\text{GeV}$
5. $-29\,\text{cm} < z_{vertex} < 31\,\text{cm}$
6. ≥ 2 e.m. clusters
7. $E_e, E_\gamma > 2\,\text{GeV}$
8. $E_e + E_\gamma > 20\,\text{GeV}$
9. $E_{t,e} - E_{t,\gamma} < 5\,\text{GeV}$
10. $E_{tot} - E_e - E_\gamma < 5\,\text{GeV}$
11. $E_{next\ cluster} < 5\,\text{GeV}$
12. $\lvert\Delta\phi - 180°\rvert < 20°$ with $\Delta\phi = \lvert\phi_e - \phi_\gamma\rvert$
13. $10° < \theta_e < 150°$
14. $6° < \theta_\gamma < 150°$
15. total number of tracks ≤ 5
16. number of tracks in cone around γ cluster=0, if $\theta \geq 35°$ number of tracks in cone around γ cluster=2 or 4, if $\theta < 35°$
17. $m_{e\gamma} > 10\,\text{GeV}$

Table 5.4: Applied cuts for the selection of elastic wide angle bremsstrahlung events.

70 GeV. The $E - p_z$ condition cuts away DIS events involving ISR as well as beam gas events. For beam gas events it is $E_{vis} - p_{z,vis} \approx m_{nucleus}$ but the residual gas mainly consists of light elements.

5) $-29\,\text{cm} < z_{vertex} < 31\,\text{cm}$
The reconstructed interaction vertex has to be in the range $-29\,\text{cm} < z_{vertex} < 31\,\text{cm}$.

6) ≥ 2 e.m. clusters
At least two electromagnetic clusters have to be found in the detector.

7) $E_e, E_\gamma > 2\,\text{GeV}$
The energies of the two most energetic clusters have to be greater than 2 GeV. This cut ensures that the electromagnetic clusters have sufficiently high energies. It keeps the final event sample free from noise clusters which could fake an electron or a photon.

8) $E_e + E_\gamma > 20\,\text{GeV}$
The sum of the two electromagnetic clusters has to be greater than 20 GeV. This cut ensures a trigger efficiency of $\sim 100\%$.

9) $E_{t,e} - E_{t,\gamma} < 5\,\text{GeV}$
The transverse energies of electron and photon should be balanced due to four-momentun conservation. Therefore a cut of $E_{t,e} - E_{t,\gamma} < 5\,\text{GeV}$ is applied to the data.

10) $E_{tot} - E_e - E_\gamma < 5\,\text{GeV}$
The total energy in the LAr calorimeter apart from the electron and photon energy has to be less than 5 GeV. This "empty detector condition" guarantees that only elastic QED Compton events are selected.

11) $E_{next\ cluster} < 5\,\mathrm{GeV}$
After electron and photon have been found the energy of the next most energetic cluster has to be less then 5 GeV. In addition to the empty detector condition it eliminates DIS background and improves the sensitivity for the elastic channel.

12) $|\Delta\phi - 180°| < 20°$ with $\Delta\phi = |\phi_e - \phi_\gamma|$
Four momentum conservation also leads to a back-to-back topology of electron and photon. Hence a cut of $|\Delta\phi - 180°| < 20°$ is applied.

13+14) $10° < \theta_e < 150°$, $6° < \theta_\gamma < 150°$
The angular cuts $10° < \theta_e < 150°$ and $6° < \theta_\gamma < 150°$ only accept events where both electromagnetic clusters lie in the LAr calorimeter. To increase the efficiency the cut on θ_γ is less stringent than the one on θ_e.

15+16) In order to ensure that the two electromagnetic clusters originate from an $e\gamma$ pair the events have to satisfy certain track requirements. Since photons are neutral no track is allowed within a cone[1] around one of the clusters if θ is greater than 35°. For $\theta < 35°$ the photons have to pass through more material. Therefore the number of tracks can be two or four, allowing for photon conversion into e^+e^- pairs. The second cluster must have a track pointing to it since the electron is charged. This requirement is already implemented in the electron finder QESCAT. The distance between the track and the cluster cog[2] has to be less than 16 cm. In addition the total number of tracks in the detector has to be less or equal five.

17)$m_{e\gamma} > 10\,\mathrm{GeV}$
The invariant mass of the $e\gamma$ system has to be greater than 10 GeV.

An event selected with these cuts is shown in fig. 5.2. The invariant mass of the $e\gamma$ system is 116.7 GeV which is the highest value among all selected events.

5.3 Comparison of data and Monte Carlo expectation

The number of events which pass the cuts described in the last section are compared with the Monte Carlo expectation from the WABGEN generator in table 5.5. The Monte Carlo events were normalized to the luminosity of the data by a factor $\mathcal{L}_{data}/\mathcal{L}_{MC}$. There is no background originating from DIS. No event from the DJANGO files mentioned in section 4.2 survived the selection requirements for QED Compton events. In addition the background originating from photon-photon scattering and photoproduction is neglected. This was justified in section 3.2.2 and 3.2.3.

In column '99^a the number of Monte Carlo events was obtained from a file generated for a proton momentum of 920 GeV and positrons as lepton type. For the Monte Carlo expectation in column '99^b a file generated with a proton momentum of 820 GeV was

[1] This is a cone with radius $R = \sqrt{\Delta\eta^2 + \Delta\phi^2} < 0.4$. The cone axis is defined by the reconstructed vertex and the center of gravity of the cluster. $\Delta\eta$ is the difference of pseudorapidity between the cone axis and the cone surface.

[2] Center of gravity

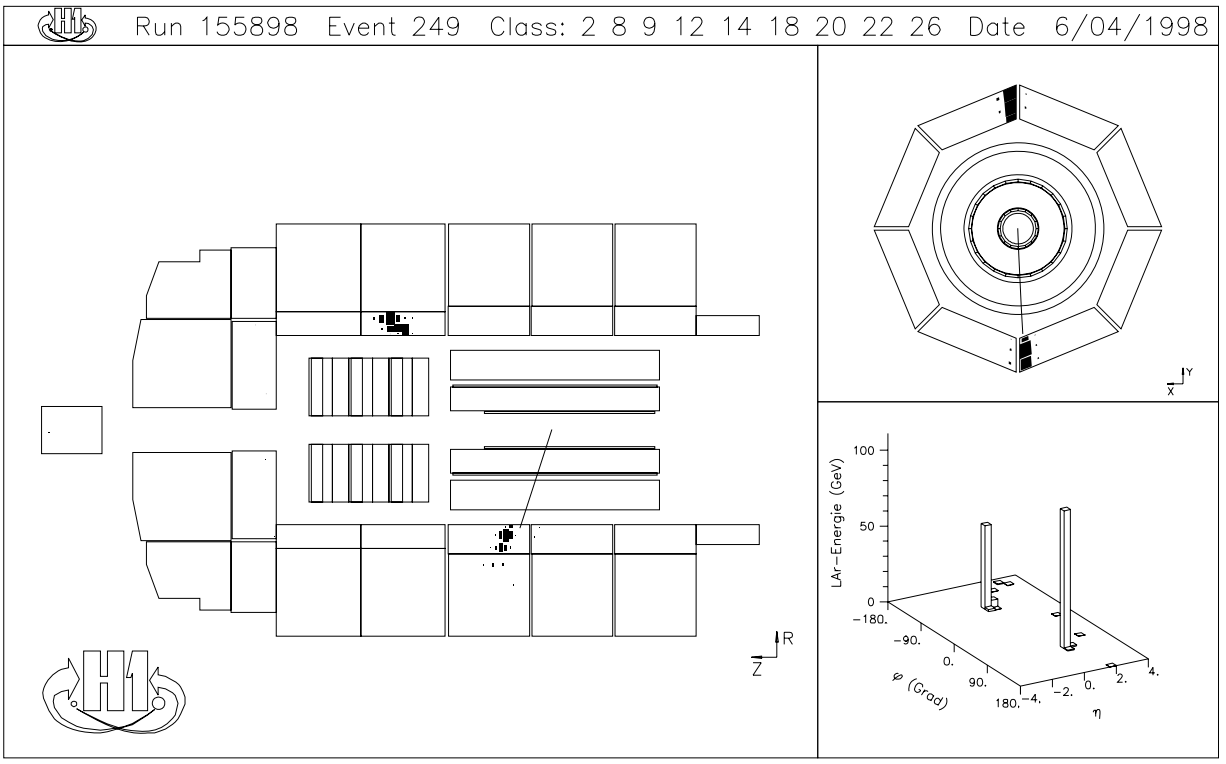

Figure 5.2: A selected event from the 1996 data. The invariant mass of the $e\gamma$ pair is 116.7 GeV. This is the highest value of $m_{e\gamma}$ among all 460 selected events.

used. Furthermore the 105 events selected from the '99 data were reweighted as described in appendix A in order to make the '99 data comparable with the information from the previous years. The numbers of column '99^b are added to the results from the period '95-'97 and shown in column c.

5.3.1 Comparison of event numbers

Table 5.3 shows that data and Monte Carlo expactation are all in agreement within the statistical error of the data. Adding the information for the different years gives a number of 470.8 observed events where 465.8 are expected from the standard model, which is an

Year	'95	'96	'97	$\sum$'95-'97	$'99^a$	$'99^b$	$\sum$'95-99^c
elastic	31.9	63.3	151.5	246.7	73.3	70.4	317.1
quasielastic	13.7	27.2	62.6	103.5	31.6	29.1	132.5
inelastic	1.7	3.4	7.4	12.5	4.8	3.4	15.9
$\sum$	47.3 ± 0.7	93.9 ± 1.5	221.5 ± 3.4	362.7 ± 3.8	109.6 ± 2.4	102.9 ± 1.6	465.5 ± 4.1
Data	54	94	207	355	105	115.8	470.8

Table 5.5: Comparison of events numbers from data and Monte Carlo (WABGEN). The 105 data events in column $'99^a$ were reweighted according to appendix A. This procedure increased the number by roughly 10% and led to the 115.8 events in column $'99^b$.

impressive agreement.

5.3.2 Distributions

In the following plots the error bars for the data points represent the statistical error. For a number of N events in a certain bin the statistical error is given by $\sqrt{N}$. The superimposed Monte Carlo distributions exclusively come from the WABGEN package. Apart from fig. 5.9 the data from '95-'97 and '99 as well as the Monte Carlo figures are simply added.

Fig. 5.3 and 5.4 show the energy distribution for electrons and photons. In fig. 5.5 and 5.6 the polar angles θ_e and θ_γ are plotted. The residual energy $E_{tot} - E_e - E_\gamma$ is depicted in fig. 5.7 and fig. 5.8 shows the histogram for $E_{next\ cluster}$. To sum up one can emphasize that the data are described by the Monte Carlo quite well.

The most important plot is the distribution of the invariant mass $m_{e\gamma}$ in fig. 5.9. Here the MC expectation was obtained from files where the proton momentum has been set to 820 GeV. Events from the '99 data sample were reweighted according to appendix A and filled into the histogram together with the data from previous years. Both the Kolmogorov-Smirnov test of section 5.3.3 and the calculation of e^* exclusion limits described in chapter 6 are based on this plot.

5.3.3 The Kolmogorov-Smirnov test

A more sophisticated test for the consistency of the data with the Monte Carlo expectation is the Kolmogorov-Smirnov test [54]. Comparing the invariant mass distrubution of fig. 5.9 between 0 GeV and 120 GeV by means of this statistical test gives a probability of 99.2% that data points and Monte Carlo are in agreement.

5.3.4 Search for new physics

An interesting test for the agreement between data and Monte Carlo expectation is the search for excited electrons in the decay channel $e^* \to e\gamma$. In the detector it has the same signature as QED Compton events. The elastic part of the cross section comprises half of the total cross section. The branching ratio for the $e\gamma$ decay channel is at least 30%.

For a single event it is impossible to decide whether it is an e^* or a QED Compton event. But if excited electrons are produced within H1, a resonance pattern would be visible in the mass spectrum of $e\gamma$ pairs. No such signal can be observed in the invariant mass plot of fig. 5.9. Instead one can derive exclusion limits for e^* production which is done in the next chapter.

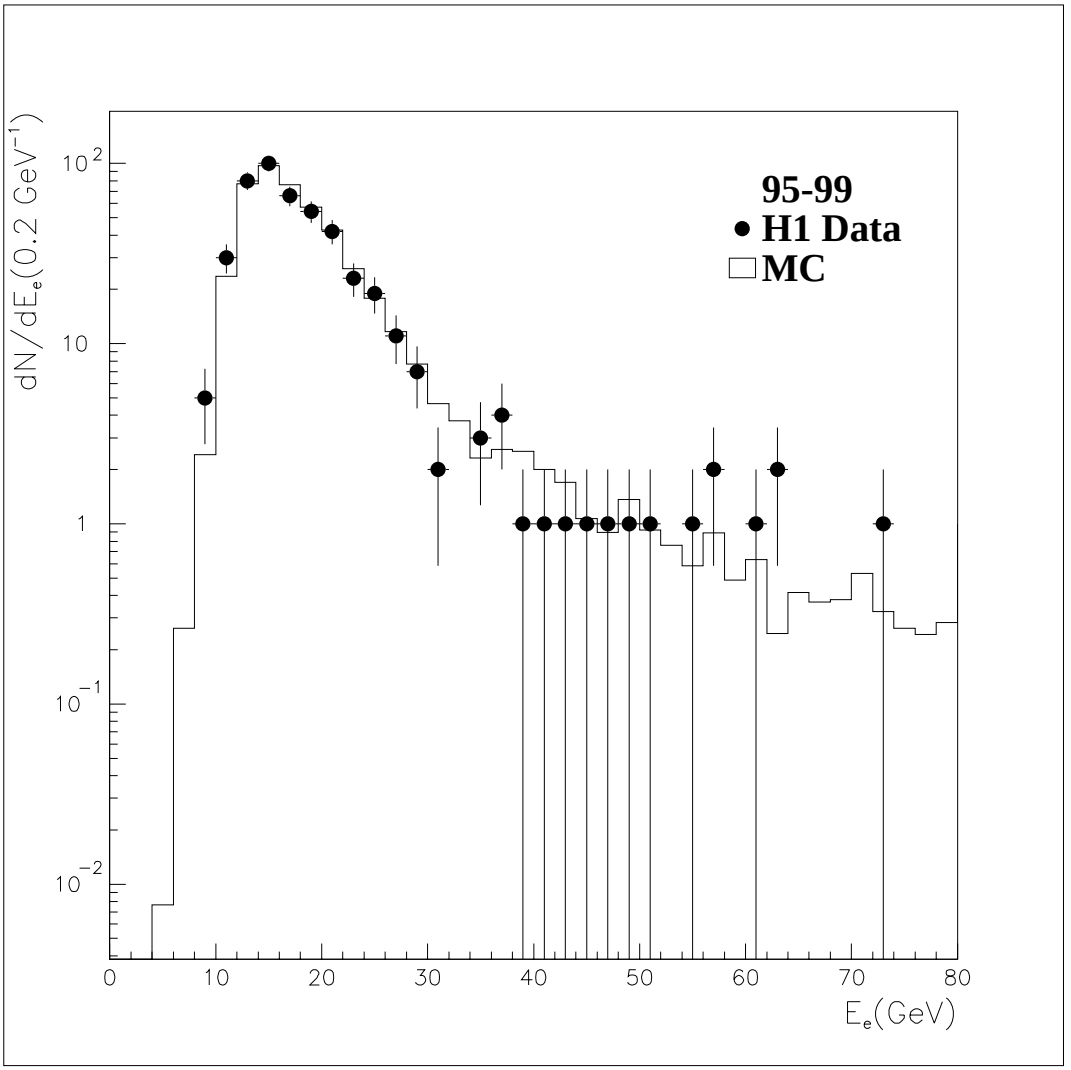

Figure 5.3: Energy distribution for E_e.

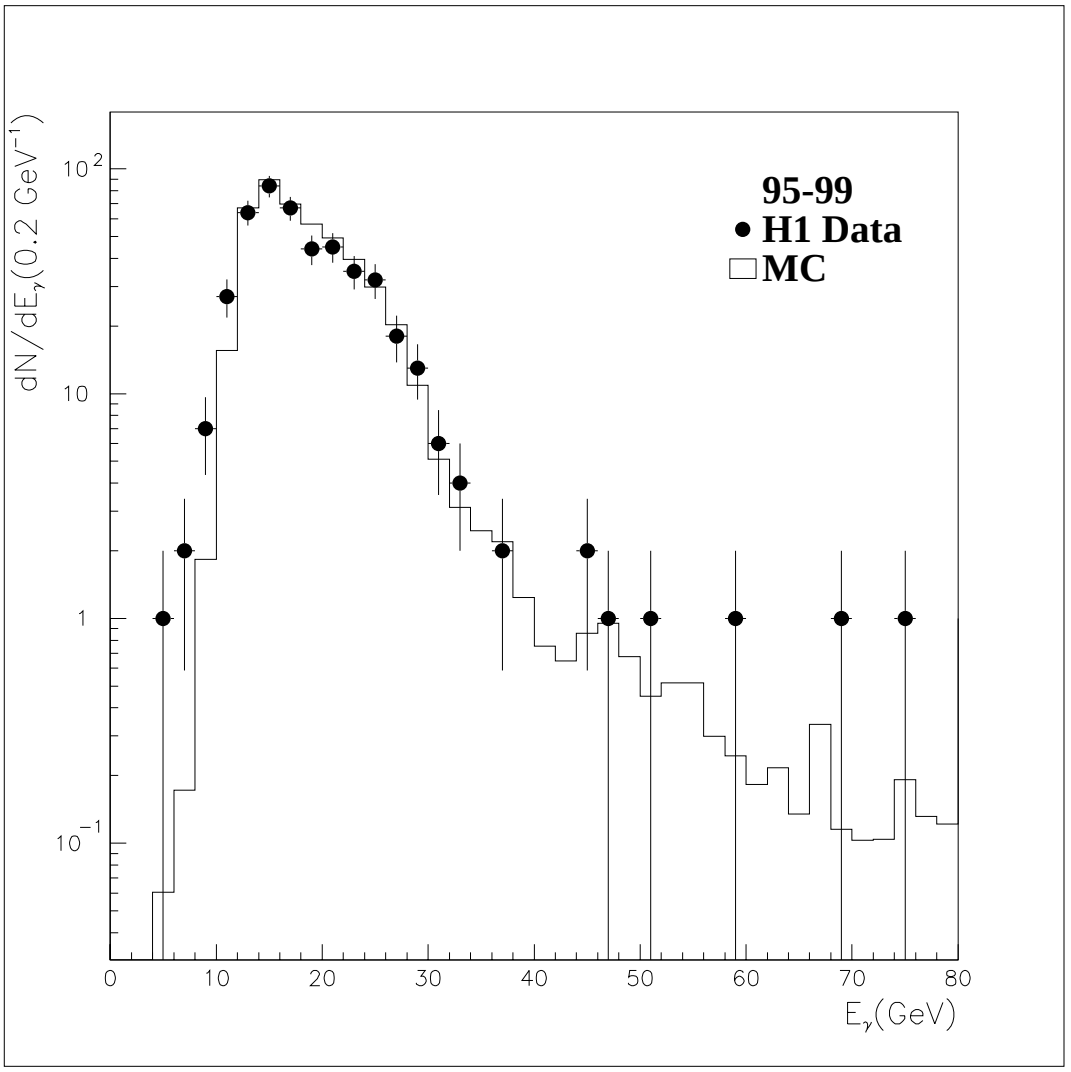

Figure 5.4: Energy distribution for E_γ.

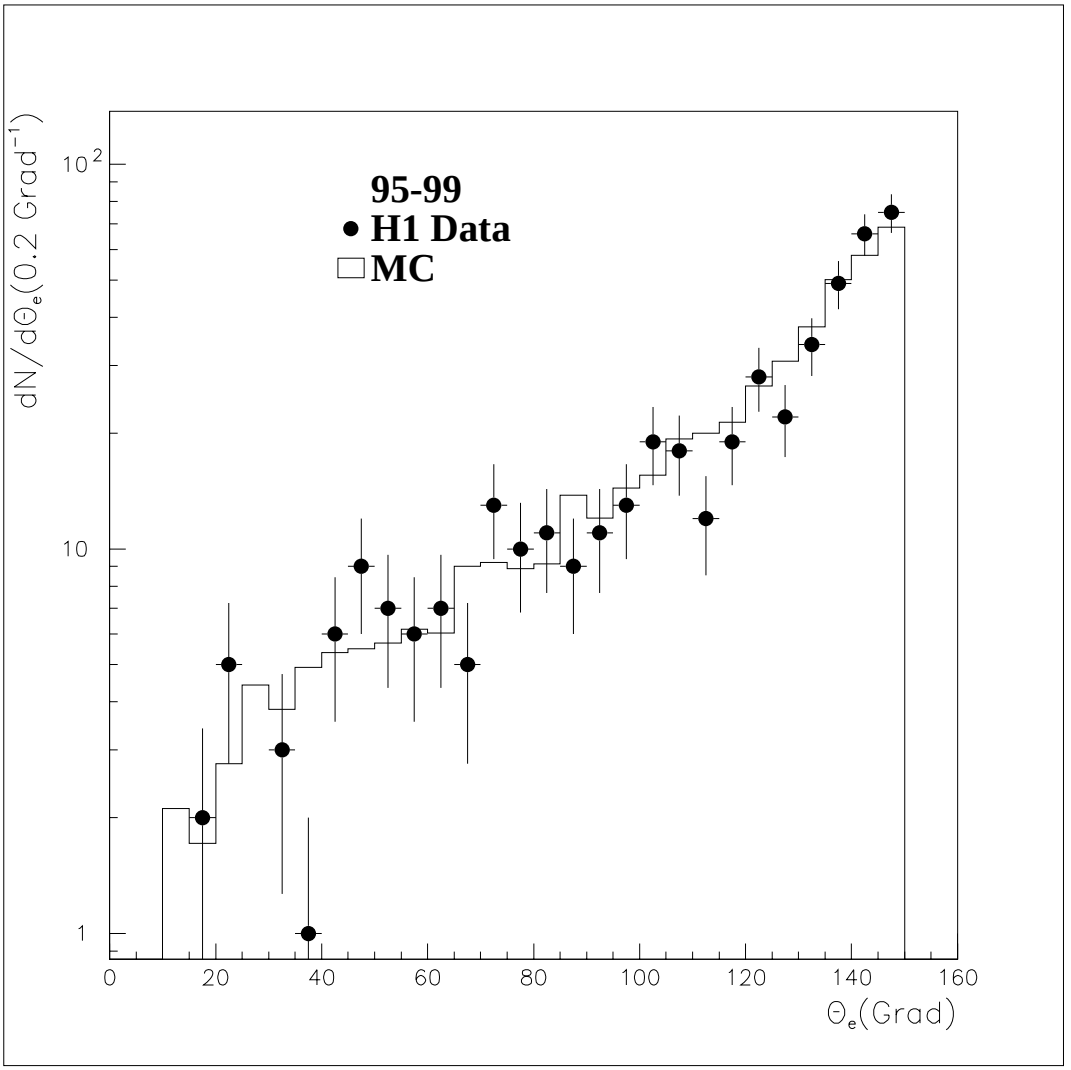

Figure 5.5: Angular distribution for θ_e.

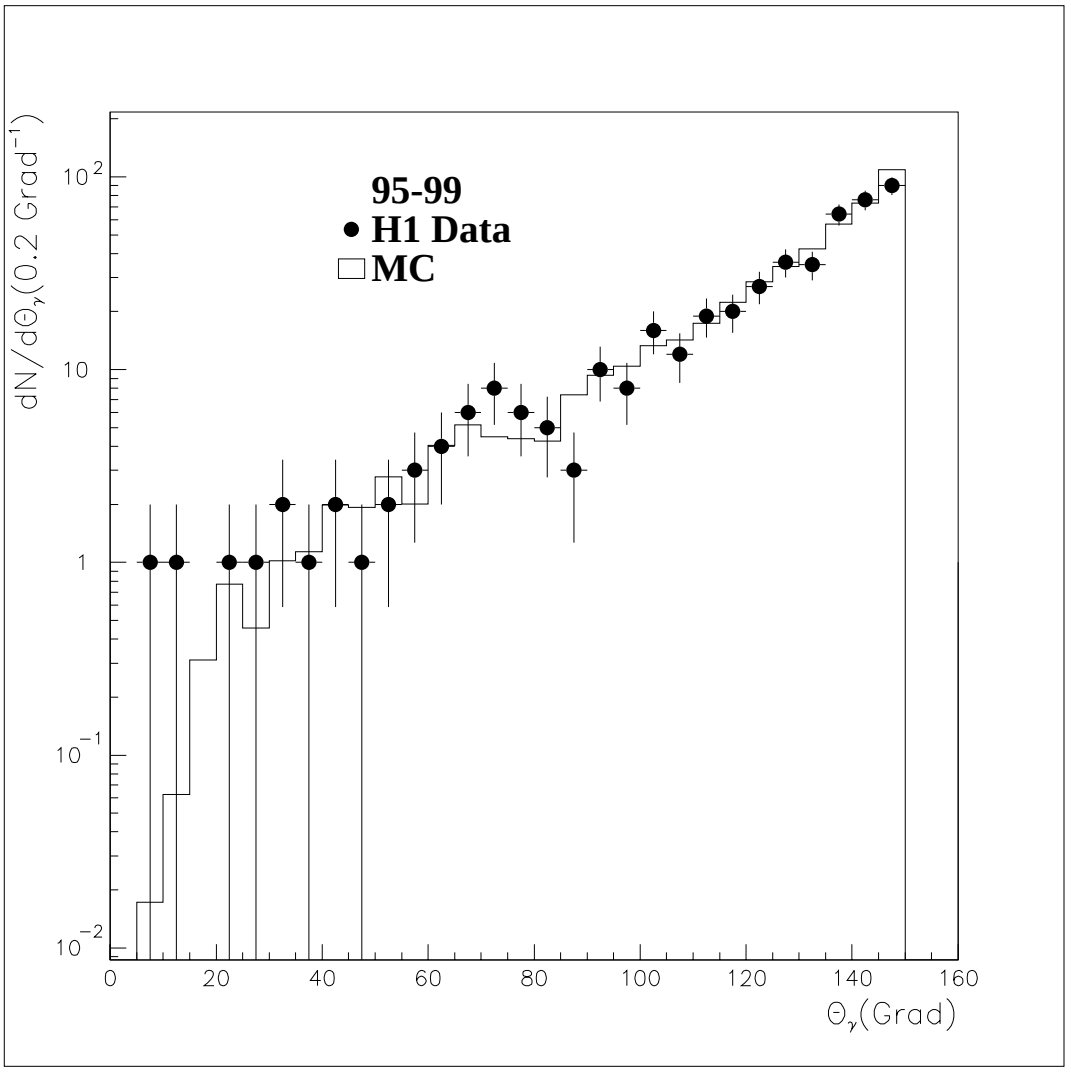

Figure 5.6: Angular distribution for θ_γ.

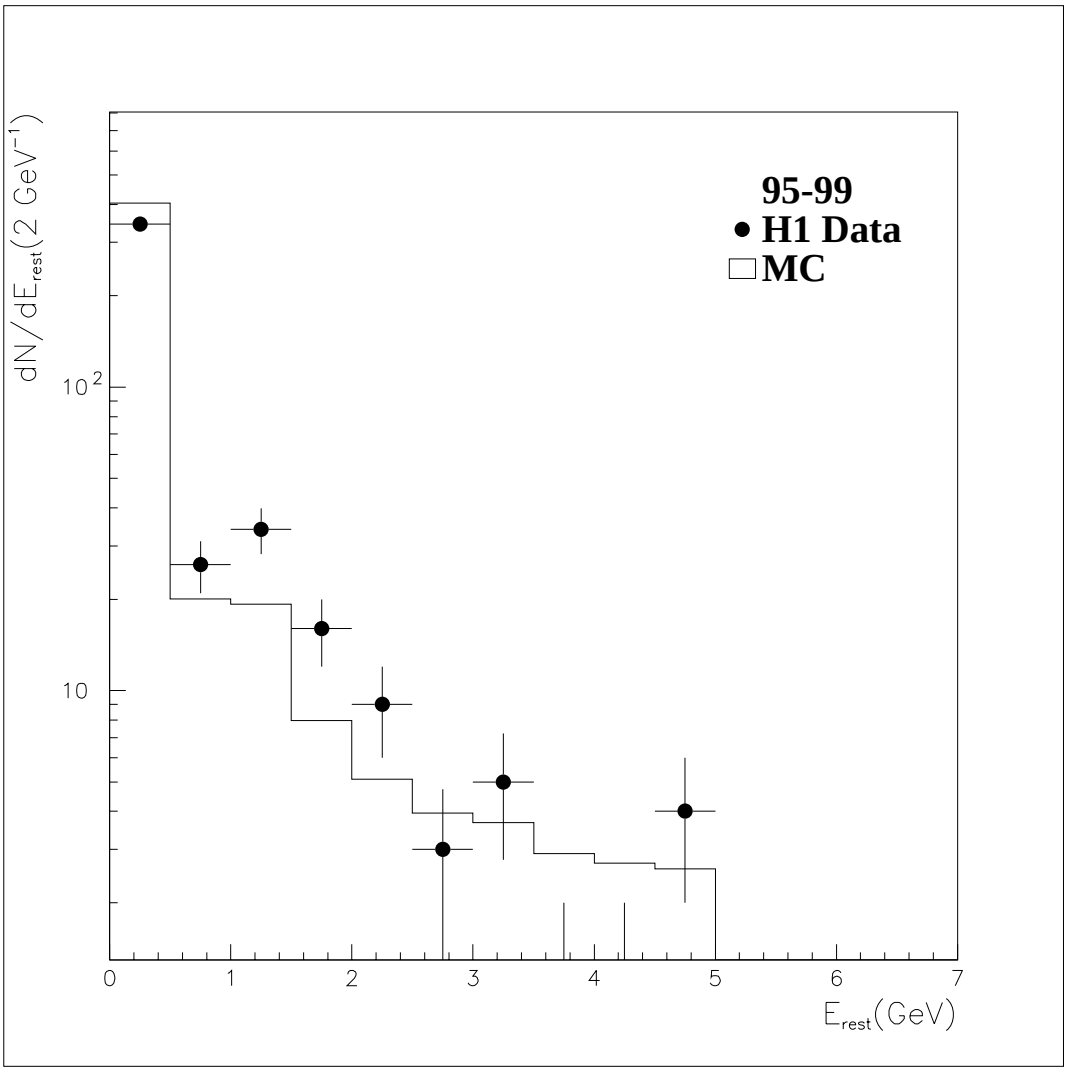

Figure 5.7: Distribution of the remaining energy $E_{tot} - E_e - E_\gamma$.

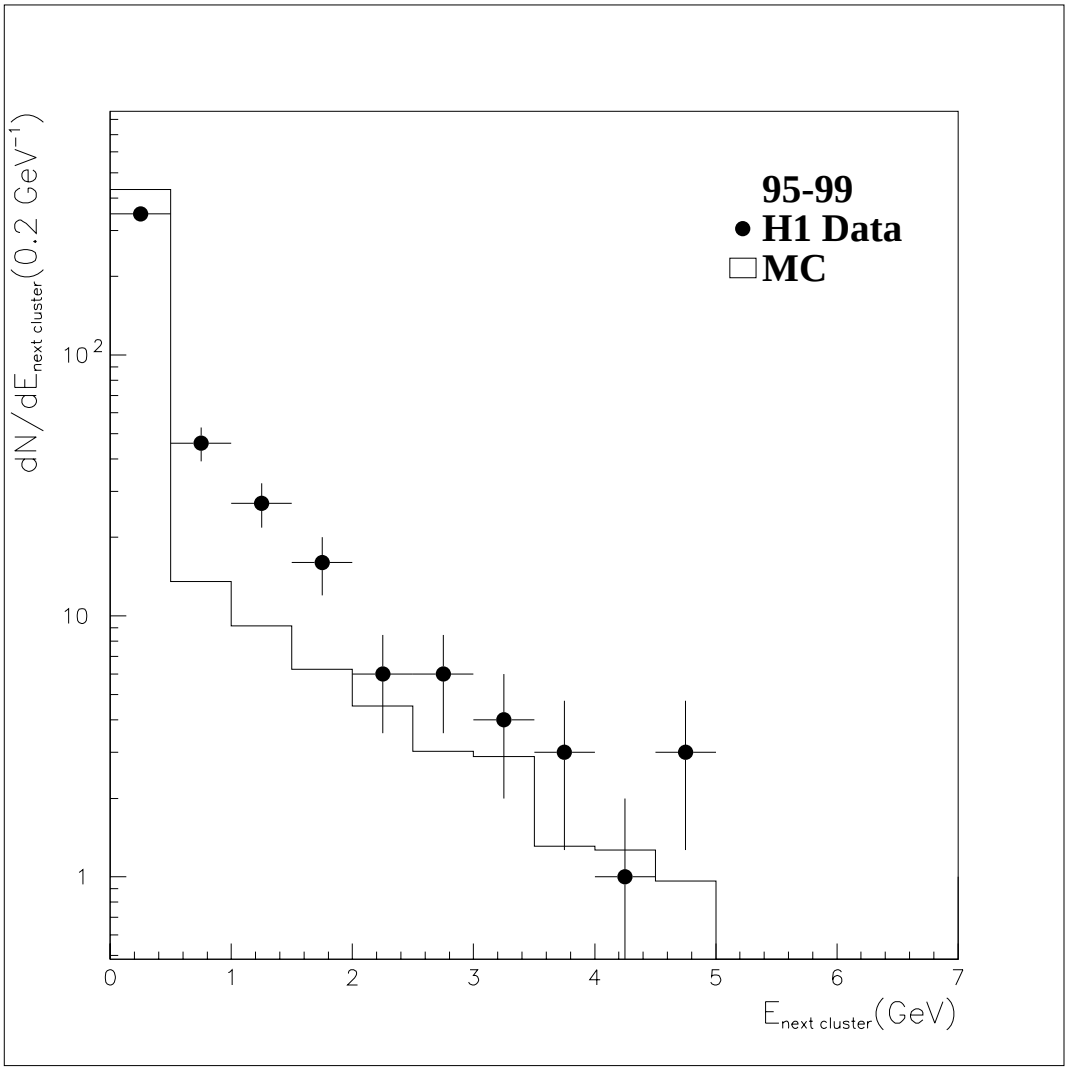

Figure 5.8: Distribution of $E_{next\ cluster}$.

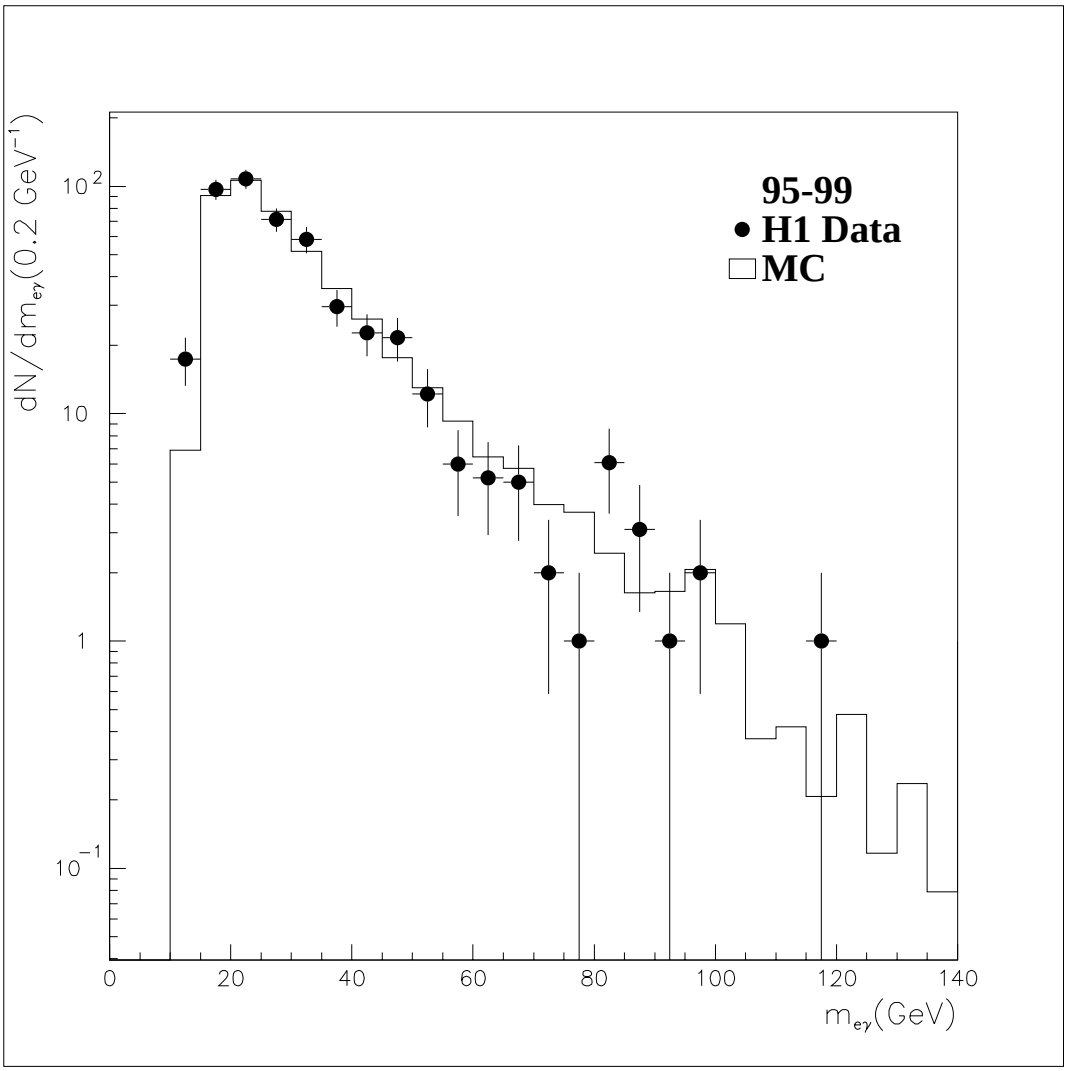

Figure 5.9: Distribution of the invariant mass $m_{e\gamma}$. The event numbers for data and Monte Carlo entries are 470.8 and 465.5 respectively.

Chapter 6

Exclusion limits for e* production

Since no significant deviation from the standard model can be found in the mass spectrum, exclusion limits on the coupling constant and the cross section of excited electrons with a certain mass will be derived in this chapter. In section 6.1 this is done using a straightforward approach whereas in section 6.2 a more precise analysis of the data is presented.

Searches for excited electrons at LEP[1] provide mass limits for single ($e^+e^- \to e^*e$) and pair production ($e^+e^- \to e^{*+}e^{*-}$) at 95% confidence level. They exclude e^* masses below 85 GeV and 91 GeV respectively [55]. These limits are close to the kinematical limit, i. e. the beam energy. At HERA it is not possible to determine a lower mass limit because in ep collisions e^* production takes place via t-channel γ/Z^0 exchange described by the magnetic coupling $\sigma^{\mu\nu}/\Lambda$.

6.1 The simple approach

Calculating a limit for the cross section is interesting because the specific model of excited fermion production only enters via the selection efficiencies. The efficiencies for other models will not be much different if one assumes the characteristics of e^* decays, the high transverse energy, only to depend on kinematics.

Since the investigated process is subject to statistical fluctuations a maximum cross section or coupling constant which can not be excluded yet can only be derived at a certain confidence level $C.L.$. The confidence level is defined such that for a large number of identical experiments a fraction $C.L.$ would give the same or a smaller result. It is conventional to calculate limits at a confidence level of 95%.

In the analysed data no event is found with an invariant mass greater then 120 GeV. At a confidence level $C.L.$ of 95% this is consistent with 3.1 observed events. From the formula

$$N = \sigma \cdot \mathcal{L}$$

one gets

$$\sigma < \frac{N}{\mathcal{L} \cdot \epsilon}$$

[1] Large electron positron collider

where ϵ is the efficiency of finding the N observed events. Table 6.1 shows an efficiency of roughly 35% for finding excited electrons with masses greater than 120 GeV. With an integrated luminosity of $41.6\,\mathrm{pb}^{-1}$ the maximum cross section for e^* production above 120 GeV is given by

$$\sigma < \frac{3.1}{41.6\,\mathrm{pb}^{-1} \cdot 0.35} = 0.21\,\mathrm{pb}$$

at 95% confidence level. This is in agreement with fig. 6.1 since no additional information is produced by the method presented in the next section.

6.2 The advanced approach using Poisson statistics

Limits are derived in the mass range from 45 GeV to 275 GeV in steps of 1 GeV. This procedure is applied in order to guarantee sensitivity in the whole parametral plane of the e^* mass and the coupling constant. For a more detailed discussion of the methods available for calculating exclusion limits the reader is refered to [56, 57].

For each decay channel and mass window the number of expected events is given by a Poisson distribution with expectation value $\mu = S + B$. S is the number of events arising from a signal, B is the number of background events. The Poisson distribution

$$P_\mu = \frac{1}{N!} \cdot \mu^N \cdot e^{-\mu}$$

gives the probability of finding N events when the expectation value is μ. The number of events S originating from e^* decay is simply given by the product of the cross section, the integrated Luminosity, the selection efficiency and BR^*, i. e.

$$S = \sigma \cdot \mathcal{L} \cdot \epsilon_{tot} \cdot BR^*.$$

BR^* is the unknown branching ratio for the decay channel $e^* \to e\gamma$. The cross section σ depends on the specific model, i. e. on the coupling constant $(c/\Lambda)^2$ and the mass of the excited electron m_{e^*}. Since the exclusion limit is always calculated for a constant m_{e^*}, the model dependence of the signal S is described by $Z = c^2/\Lambda^2 \cdot BR^*$. One gets

$$S(Z) = \sigma_0 \cdot \frac{\Lambda_0^2}{c_0^2} \cdot \mathcal{L} \cdot \epsilon_{tot} \cdot Z$$

where σ_0 is the cross section resulting from a coupling constant c_0/Λ_0. Usually exclusion limits for excited lepton production are published as $\sqrt{Z} = \frac{c}{\Lambda} \cdot \sqrt{BR^*}$ over a certain mass range. This convention will be kept here.

6.2.1 The confidence level

Taking into account just one decay channel is the most simple case for the calculation of a confidence level. In our case it is defined by

$$C.L. = \frac{\int_0^{Z_0} dZ\, P(S(Z) + B|N)}{\int_0^{\infty} dZ\, P(S(Z) + B|N)}. \tag{6.1}$$

$P(S(Z)+B|N)$ is the probability of having found $S(Z)$ e^* events among N candidates and B background events. By means of the Bayes' theorem [58] the posteriory probability $P(S(Z)+B|N)$ can be combined with

$$P_\mu = P(N|S(Z)+B) = \frac{1}{N!} \cdot (S(Z)+B)^N \cdot e^{-(S(Z)+B)}$$

and the a priory probability $P(S)$:

$$P(S(Z)+B|N) \propto P(N|S(Z)+B) \cdot P(S).$$

The unknown probability $P(S)$ is assumed to be equally distributed. Due to the division in equation 6.1 no normalization is required for $P(S(Z)+B|N)$. One can insert

$$P(S(Z)+B|N) = \frac{1}{N!} \cdot (S(Z)+B)^N \cdot e^{-(S(Z)+B)}$$

and solve the equation numerically. Limits will be calculated for the product $Z' = \sigma \cdot BR^*$ of the cross section and the unknown branching ratio. The expected signal is given by

$$S(Z') = \mathcal{L} \cdot \epsilon_{tot} \cdot Z'.$$

Of course the calculation of an exclusion limit for Z' is done in the same way as was described for Z.

6.2.2 Determination of selection efficiencies

In order to calculate exclusion limits one has to determine the selection efficiency for the investigated process. For the reaction $e^* \to e\gamma$ this was done by means of the COMPOS generator. Events with e^* masses of 50 GeV, 75 GeV, 100 GeV, 150 GeV, 200 GeV and 250 GeV were generated with the parameters listed in section 4.3. The number of simulated events for each mass point is given in table 6.1. The selection cuts for wide angle bremsstrahlung from table 5.4 were applied. Then the invariant mass of the remaining events was plotted and a mass range $\Delta m_{e\gamma}$ was defined such that only few events lie outside of this mass window. Above an e^* mass of 120 GeV it is sufficient to set the lower limit of $\Delta m_{e\gamma}$ to 120 GeV since no event exceeding this value was found in the data. The upper limit was set to be 300 GeV. The total selection efficiencies seem to be low but are sufficiently high to perform a search for excited electrons.

6.2.3 Exclusion limit on the cross section

Fig. 6.1 shows the exclusion limit on $\sigma \cdot BR^*$ at 95% confidence level. It has to be noted that this is a limit for the total production of excited electrons and not just for the elastic channel. The reason is that the analysed COMPOS files were generated without constraining the production process. The selection efficiencies were taken from table 6.1. Cross sections above the curve are excluded. The fluctuations below 100 GeV are due to the fact that e^* candidates were found in this area. In total cross sections of the order 0.3 pb are excluded. This value improves the limit from ref. [19] by a factor of ~ 3 due to the gain in luminosity.

M_{e^*} [GeV]	50	75	100	150	200	250
# simulated events	1982	1975	1974	1966	1968	1986
# selected events	770	933	871	779	694	590
ϵ_{sel} [%]	38.85	47.24	44.12	39.62	35.26	29.71
$\Delta m_{e\gamma}$ [GeV]	45-52	68-78	94-104	>120	>120	>120
# events in $\Delta m_{e\gamma}$	754	920	853	779	694	590
ϵ_{tot} [%]	38.04	46.58	43.21	39.62	35.26	29.71

Table 6.1: Efficiencies for the selection of e^* events generated with COMPOS.

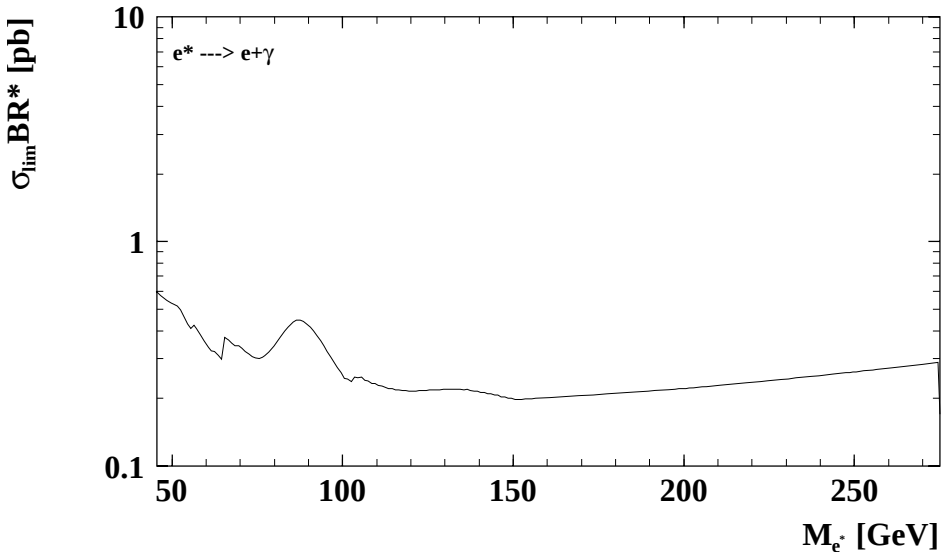

Figure 6.1: Exclusion limit on the e^* production cross section times the branching ratio BR^* as a function of m_{e^*}. The confidence level is 95%.

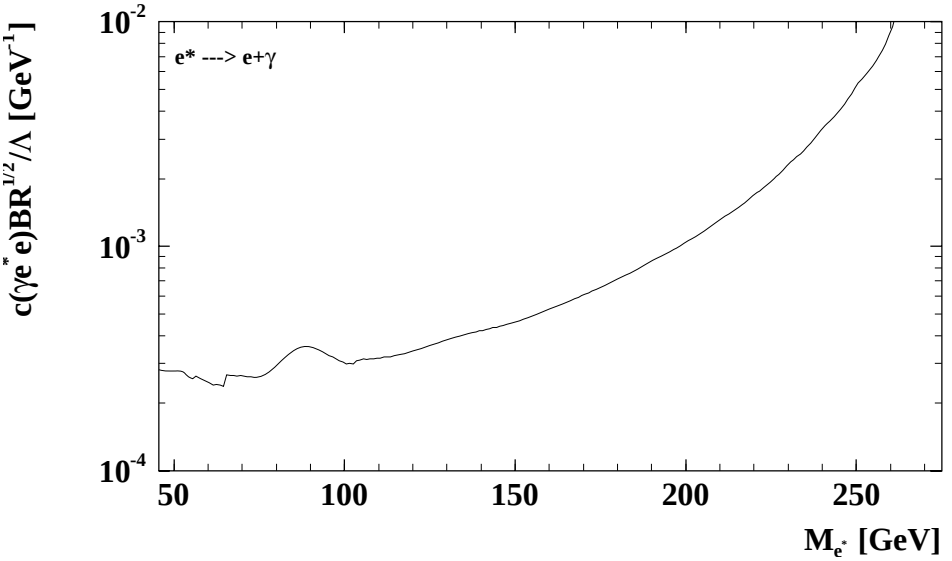

Figure 6.2: Exclusion limit on $c/\Lambda \cdot \sqrt{BR^*}$ for e^* masses between 45 GeV and 250 GeV at 95% confidence level.

6.2.4 Exclusion limit on the coupling constant

The exclusion limit on the coupling costant c/Λ times the square root of the branching ratio $\sqrt{BR^*}$ at 95% confidence level is shown in fig. 6.2. Again the area above the curve is excluded by the experimental data. It reflects the selection efficiencies and the number of e^* candidates. The model dependent production cross section enters as well, i. e. another model for excited fermion production would yield a different curve. Compared to ref. [19] the limit improves by a factor ~ 2 because of the increased luminosity.

Chapter 7

Conclusion and Outlook

Conclusion

The presented study deals with the QED process of wide angle bremsstrahlung $ep \to ep\gamma$ at the ep collider HERA. It is based on $32.4\,\mathrm{pb}^{-1}$ of e^+p data with a center-of-mass energy of 300 GeV collected from 1995 to 1997 and $9.2\,\mathrm{pb}^{-1}$ of e^-p data with a center-of-mass energy of 313 GeV from 1999. Events which fulfill the expected topology, i. e. an electron and a photon in the main detector without major hadronic activity are selected and compared with the standard model expectation.

During the course of this study it was tried to extend the search for two electromagnetic clusters to the backward calorimeter SPACAL. The application of the electron finder QESCAT produced strange results. The code was found to have a bug in the routine which sorts the electromagnetic SPACAL clusters according to their energy. The bug had the effect of double counting as well as superseding electron candidates. The implementation of a bug fix developed for [59] was unsuccessful. Own code had to be written to read out the SPACAL memory banks and sort the clusters w. r. t. their energy. Due to the lack of time it was decided not to include the SPACAL into the analysis and to concentrate an the LAr calorimeter instead.

An excellent agreement between the data and the Monte Carlo generator WABGEN is found for both event numbers and kinematic distributions. Background from other reactions is neglected.

The data offer the interesting opportunity to search for new physics. Single excited electrons e^* predicted by compositeness models could be produced via t-channel γ/Z^0 exchange. The subsequent decay $e^* \to e\gamma$ would produce a resonance peak in the invariant mass plot. No such resonance pattern can be found in the data. Limits for the production cross section and the coupling constant are derived at 95% confidence level and improve previous results.

Outlook

An improvement for future analyses would be the inclusion of events having one electromagnetic cluster in the LAr calorimeter and one in the SPACAL as well as events with two electromagnetic SPACAL clusters. Extending the analysis to the lowest invariant masses

accessible with H1 can be achieved by taking into account the VLQ[1]. Due to the increased cross section an alternative luminosity measurement apart from the H1 luminosity system seems to be feasible.

By considering the FPS[2] one could verify, whether the empty detector condition is an appropriate criterion to distinguish elastic from inelastic QED Compton events. In 1998 the performance of the FPS was rather poor. Due to the high background rate within HERA the roman pots could hardly be moved. The vertical station only collected 3% of the H1 luminosity, the horizontal station recorded 7%. During previous years these numbers have been similar. In 1999 the FPS performance increased significantly because of improved background conditions.

The exclusion limits presented in chapter 6 can be improved simply by analysing more data. Increasing the integrated luminosity by a factor N improves the exclusion limit for the cross section by the same factor, if no additional e^* candidates are found. The limit on the coupling constant would improve by a factor $\sqrt{N}$. As a first step the data collected during the run periods of 1994, 1998 and the remaining 1999 e^+ data could be analyzed. From the year 2000 to 2001 a major luminosity upgrade for the H1 detector is scheduled. Afterwards the event rate will increase by a factor of five. Among other measures, this will be achieved by new focusing magnets for the electron and the proton beam. The opportunity to establish deviations from the standard model will improve significantly. In addition one could change the selection cuts in order to increase the e^* selection efficiency of roughly 35%. On the other hand this could increase the number of selected background events.

[1] Very Low Q^2 Spectrometer
[2] Forward Proton Spectrometer

Appendix A

The reweighting procedure

In order to make the events which were found in the '99 data sample ($E_p = 920\,\mathrm{GeV}$) comparable with events from previous years ($E_p = 820\,\mathrm{GeV}$) the following method was applied.

The cross section for wide angle bremsstrahlung can be split up into two factors: a flux factor $f_{\gamma/p}(x) \sim \ln E_p/m_p$ and the cross section for Compton scattering which is proportional to $1/\hat{s}$. One gets

$$\frac{d\sigma}{d\hat{t}\,dx} = f_{\gamma/p}(x) \cdot \frac{1}{\hat{s}} \cdot g(\hat{t}) \tag{A.1}$$

The variables are defined as

$$\begin{aligned} x &= \frac{E_\gamma}{E_p}, \\ \hat{s} &= 4x E_e E_p = m_{e\gamma}^2, \\ \hat{t} &= (e - e')^2. \end{aligned} \tag{A.2}$$

where e and e' are the four-momenta of the incoming and outgoing electron respectively. One can rewrite eqn. A.1 to give

$$\frac{d\sigma}{d\hat{t}\,dx} = \frac{1}{E_p} \cdot \ln\frac{E_p}{m_p} \cdot f(x, \hat{t}). \tag{A.3}$$

The functions $g(\hat{t})$ and $f(x, \hat{t})$ are not specified since they do not enter the algorithm. When an event was selcted in the '99 data x was calculated according to eqn. A.2, i. e.

$$x = \frac{m_{e\gamma}^2}{4E_e E_p}$$

with $E_e = 27.5\,\mathrm{GeV}$ and $E_p = 920\,\mathrm{GeV}$. With this value of x the new invariant mass was then calculated again by means of eqn. A.2 where E_p was set to 820 GeV. Finally the event was filled into the histogram of fig. 5.9. The weight w follows from eqn. A.3 by the rule of proportion and is given by

$$w = \frac{\frac{1}{820\,GeV} \cdot \ln\frac{820\,GeV}{m_p}}{\frac{1}{920\,GeV} \cdot \ln\frac{920\,GeV}{m_p}} = 1.1032\,.$$

Therefore in table 5.3 the number of 105 events in colomn '99^a increases by $\sim 10\%$ to give 115.8 events in column '99^b.

List of Figures

List of Tables

Bibliography

[1] Roger Penrose. *The Emperor's New Mind: Concerning Computers, Minds, and the Laws of Physics*. Oxford University Press, November 1989. ISBN 0198519737.

[2] C. N. Yang and R. L. Mills. Conservation of isotopic spin and isotopic gauge invariance. *Phys. Rev.*, 96:191, 1954.

[3] Steven Weinberg. *The Quantum Theory of Fields*, volume 1-3. Cambridge University Press, 1995. ISBN 0521550017.

[4] Michael E. Peskin and Daniel V. Schroeder. *An Introduction to Quantum Field Theory*. Perseus Press, September 1995. ISBN 0201503972.

[5] S. L. Glashow. Partial symmetries of weak interactions. *Nucl. Phys.*, 22:579, 1961.

[6] J. Goldstone, A. Salam, and S. Weinberg. Broken symmetries. *Phys. Rev.*, 127:965, 1962.

[7] S. Weinberg. A model of leptons. *Phys. Rev. Lett.*, 19:1264–1266, 1967.

[8] P. W. Higgs. Broken symmetries, massless particles and gauge fields. *Phys. Lett.*, 12:132, 1964.

[9] P. W. Higgs. Spontaneous symmetry breakdown without massless bosons. *Phys. Rev.*, 145:1156, 1966.

[10] Charles W. Misner, John A. Wheeler, and Kip S. Thorne. *Gravitation*. W H Freeman & Co, September 1973. ISBN 0716703440.

[11] P. H. Frampton and B. H. Lee. SU(15) grand unification. *Phys. Rev. Lett.*, 64:619, 1990.

[12] P. B. Pal. Mass scales and symmetry breaking in SU(15) grand unification. *Phys. Rev.*, D43:236–240, 1991.

[13] Michael E. Peskin in [60]. Compositeness of quarks and leptons. page 880. QCD161:I71:1981.

[14] Ch. Berger. *Teilchenphysik - Eine Einführung*. Springer-Verlag, 1992. Berlin, Heidelberg.

[15] J. Wess and B. Zumino. Supergauge transformations in four-dimensions. *Nucl. Phys.*, B70:39, 1974.

[16] J. L. Hewett and T. G. Rizzo. Low-energy phenomenology of superstring inspired E(6) models. *Phys. Rept.*, 183:193, 1989.

[17] J. Louis. Duality in string theory and some phenomenological implications. Talk within the DESY seminar, December 8th 1998.

[18] T. Köhler. *Suche nach angeregte Leptonen mit dem H1 Detektor*. PhD thesis, RWTH-Aachen, February 1995. PITHA 95/6.

[19] W. Rottkirchen. Weitwinkel-Bremsstrahlung und angeregte Elektronen im H1 Detektor. Diploma thesis, RWTH-Aachen, May 1998.

[20] I. Abt et al. The H1 detector at HERA. (Updated version). *Nucl. Instrum. Meth.*, A386:310, 1997.

[21] H. Bethe and W. Heitler. *Proc. Roy. Soc.*, A146:83, 1934.

[22] Ch. Berger and P. Kandel in [61]. A new generator for wide angle bremsstrahlung. pages 596–600, 1999.

[23] R. Gastmans and T. T. Wu. *The Ubiquitous Photon: Helicity Method for QED and QCD*. Clarendon Press, September 1990. ISBN 0198520433.

[24] L. W. Mo and Y. S. Tsai. Radiative corrections to elastic and inelastic e p and mu p scattering. *Rev. Mod. Phys.*, 41:205–235, 1969.

[25] A. A. Akhundov, D. Yu. Bardin, C. Burdik, P. Kh. Khristova, and L. V. Kalinovskaya. Contribution of the radiative tail from the elastic peak to deep inelastic scattering at hera. *Z. Phys.*, C45:645, 1990.

[26] A. Courau and P. Kessler. QED Compton scattering in high-energy electron - proton collisions. *Phys. Rev.*, D46:117–124, 1992.

[27] R. Hofstadter. *Rev. Mod. Phys.*, 28:214, 1956.

[28] A. Mendez. QCD predictions for semiinclusive and inclusive leptoproduction. *Nucl. Phys.*, B145:199, 1978.

[29] P. Kessler. *Nuovo Cimento*, 17:809, 1960.

[30] V. M. Budnev, I. F. Ginzburg, G. V. Meledin, and V. G. Serbo. The two photon particle production mechanism. Physical problems. Applications. Equivalent photon approximation. *Phys. Rept.*, 15:181–281, 1974.

[31] Bernd A. Kniehl. Elastic e p scattering and the Weizsacker-Williams approximation. *Phys. Lett.*, B254:267–273, 1991.

[32] Torbjorn Sjostrand. Pythia 5.7 and jetset 7.4: Physics and manual. 1995. hep-ph/9508391, CERN-TH 7112/93.

[33] F. W. Brasse et al. *Nucl. Phys.*, B39:421, 1972.

[34] F. E. Low. Heavy electrons and muons. *Phys. Rev. Lett.*, 14:238–239, 1965.

[35] N. Cabibbo, L. Maiani, and Y. Srivastava. Anomalous Z decays: Excited leptons? *Phys. Lett.*, 139B:459, 1984.

[36] J. Kuhn and P. Zerwas. Excited quarks and leptons. *Phys. Lett.*, 147B:189, 1984.

[37] F. M. Renard. Scalar boson production and decay in composite models. *Phys. Lett.*, 126B:59, 1983.

[38] A. De Rujula, L. Maiani, and R. Petronzio. Search for excited quarks. *Phys. Lett.*, 140B:253, 1984.

[39] K. Hagiwara, D. Zeppenfeld, and S. Komamiya. Excited lepton production at LEP and HERA. *Z. Phys.*, C29:115, 1985.

[40] F. M. Renard. Limits on masses and couplings of excited electrons and muons. *Phys. Lett.*, 116B:264, 1982.

[41] F. del Aguila, A. Mendez, and R. Pascual. On the g-2 and the p anti-p $\rightarrow$ Z0 $\rightarrow$ lepton+ lepton- gamma events. *Phys. Lett.*, 140B:431, 1984.

[42] Mahiko Suzuki. Anomalous Z decays and g-2 of electron. *Phys. Lett.*, 143B:237, 1984.

[43] A. D. Martin, R. G. Roberts, and W. J. Stirling. *Phys. Lett.*, 306B:145, 1993. Erratum 309B (1993) 492.

[44] F. Boudjema, A. Djouadi, and J. L. Kneur. Excited fermions at e+ e- and e p colliders. *Z. Phys.*, C57:425–450, 1993.

[45] M. Spira. Diploma thesis, RWTH-Aachen, July 1989.

[46] C. Berger, P. Fuhrhmann, F. Raupach, M. Spira, and P. Zerwas in [62]. Excited leptons at LEP / LHC. volume 2, pages 1014–1021, 1990. PITHA 90/30, RWTH-Aachen, December 1990.

[47] R. Brun, F. Bruyant, M. Maire, A. C. McPherson, and P. Zanarini. GEANT 3. CERN-DD/EE/84-1.

[48] V. D. Barger and R. J. N. Phillips. *Collider Physics*, volume 71 of *Frontiers in Physics*. Addison Wesley, 1982. ISBN 0201058766.

[49] S. Kawabata. *Comp. Phys. Commun.*, 41:127, 1986.

[50] G. A. Schuler and H. Spiesberger in [63]. DJANGO 1.0: The Interface for the event generators HERACLES and LEPTO. volume 3, pages 1419–1432, 1991.

[51] T. Köhler in [63]. COMPOS 1.40 — Exotic processes at HERA: the event generator COMPOS. volume 3, page 1526, 1991.

[52] T. Köhler. Diploma thesis, RWTH-Aachen, June 1989.

[53] J. Scheins. PhD thesis in preparation.

[54] W. H. Press, S. A. Teukolsky, W. T. Vetterling, and B. P. Flannery. *Numerical Recipes in FORTRAN*. Cambridge University Press, 1992. ISBN 052143064X.

[55] C. Caso et al. Review of particle physics. *Eur. Phys. J.*, C3:1–794, 1998.

[56] K. Hikasa et al. Review of particle properties. particle data group. *Phys. Rev.*, D45:S1, 1992.

[57] H. Mönsch. PhD thesis, RWTH-Aachen, January 1991. PITHA 91/2.

[58] A. G. Fodesen, O. Skjeggstad, and H. Tofte. *Probability and Statistics in Particle*. 1979. Universitetsforlaget, Oslo.

[59] R. Stamen. Analyse quasireeller QED-Compton-Ereignisse. Diploma thesis, University Dortmund, March 1998.

[60] W. Pfeil, editor. *Xth International Symposium on Lepton and Photon Interactions at High Energy. Proceedings*, Bonn Univ., Phys. Inst., West Germany, Aug 24-29 1981.

[61] A. T. Doyle, G. Grindhammer, G. Ingelmann, and H. Jung, editors. *Monte Carlo generators for HERA physics. Proceedings, Workshop*, DESY Hamburg, 1999. DESY-PROC-1999-02, ISSN 1435-8077.

[62] G. Jarlskog and D. Rein, editors. *Large Hadron Collider. Proceedings, Workshop*, Aachen, Germnay, October 4-9 1990. CERN-90-10.

[63] W. Buchmüller and G. Ingelmann, editors. *Physics at HERA. Proceedings, Workshop*, DESY Hamburg, October 1991.

Danksagung

Mein erster Dank gilt Herrn Prof. Dr. Christoph Berger, der es mir ermöglichte diese Arbeit am DESY durchzuführen und so die Arbeit in einer internationalen Kollaboration kennenzulernen. Herr Prof. Dr. Flügge war so freundlich das Koreferat zu übernehmen. Außerdem bedanke ich mich bei allen Mitgliedern der Aachener Arbeitsgruppe die zum Gelingen dieser Arbeit beigetragen haben. Mein besonderer Dank gilt Thomas Hadig, der mir bei Softwareproblemen stets hilfreich zur Seite stand.

Hamburg, Dezember 1999 *Martin Hennecke*